

Cuspy dark matter density profiles in massive dwarf galaxies

Lauren H. Cooke,^{1,2} Rebecca C. Levy,^{1,3*}† Alberto D. Bolatto,^{1,4,5,6} Joshua D. Simon,⁷
 Andrew B. Newman,⁷ Peter Teuben,¹ Brandon D. Davey,^{1,8} Melvyn Wright,⁹ Elizabeth Tarantino,¹
 Laura Lenkić,^{1,10} and Vicente Villanueva¹

¹Department of Astronomy, University of Maryland, College Park, MD 20742, USA

²Holton-Arms School, Bethesda, MD 20817, USA

³Steward Observatory, University of Arizona, Tucson, AZ 85721, USA

⁴Joint Space-Science Institute, University of Maryland, College Park, MD 20742, USA

⁵Visiting Scholar at the Flatiron Institute, Center for Computational Astrophysics, NY 10010, USA

⁶Visiting Astronomer, National Radio Astronomy Observatory, VA 22903, USA

⁷Observatories of the Carnegie Institution for Science, Pasadena, CA 91101, USA

⁸Department of Physics, University of South Florida, Tampa, FL 33620, USA

⁹Department of Astronomy, University of California, Berkeley, CA 94720, USA

¹⁰SOFIA Science Center, USRA, NASA Ames Research Center, M.S. N232-12, Moffett Field, CA 94035, USA

Accepted 2022 February 28. Received 2022 February 28; in original form 2021 June 21

ABSTRACT

Rotation curves of galaxies probe their total mass distributions, including dark matter. Dwarf galaxies are excellent systems to investigate the dark matter density distribution, as they tend to have larger fractions of dark matter compared to higher mass systems. The core-cusp problem describes the discrepancy found in the slope of the dark matter density profile in the centres of galaxies (β^*) between observations of dwarf galaxies (shallower cores) and dark matter-only simulations (steeper cusps). We investigate β^* in six nearby spiral dwarf galaxies for which high-resolution CO $J = 1 - 0$ data were obtained with ALMA. We derive rotation curves and decompose the mass profile of the dark matter using our CO rotation curves as a tracer of the total potential and 4.5 μm photometry to define the stellar mass distribution. We find $\langle \beta^* \rangle = 0.6$ with a standard deviation of ± 0.1 among the galaxies in this sample, in agreement with previous measurements in this mass range. The galaxies studied are on the high stellar mass end of dwarf galaxies and have cuspiest profiles than lower mass dwarfs, in agreement with other observations. When the same definition of the slope is used, we observe steeper slopes than predicted by the FIRE and NIHAO simulations. This may signal that these relatively massive dwarfs underwent stronger gas inflows toward their centres than predicted by these simulations, that these simulations over-predict the frequency of accretion or feedback events, or that a combination of these or other effects are at work.

Key words: galaxies: kinematics and dynamics – galaxies: ISM – galaxies: dwarf – dark matter

1 INTRODUCTION

Dwarf galaxies have proven to be important laboratories to test principles of current dark energy and cold dark matter cosmology (ΛCDM), despite their difficulty to observe (e.g., Bullock & Boylan-Kolchin 2017; Lelli 2022). Cosmological simulations of cold dark matter predict a cusp-like dark matter density distribution near galaxy centres, meaning the density has a power-law slope (β) between 1 and 1.5 (e.g., Navarro et al. 1996b; Moore et al. 1999)¹. The most well-known form of this density distribution is the Navarro-Frenk-White (NFW) profile (Navarro et al. 1996b). Observational studies of dwarf galaxies, however, show that central density profiles range from flat

core-like distributions ($\beta \approx 0$) to the cusp-like profiles expected from dark matter-only simulations (see e.g., De Blok et al. 2001a,b; De Blok & Bosma 2002; Simon et al. 2005; Oh et al. 2011, 2015; Adams et al. 2014; Relatores et al. 2019a,b). This discrepancy in the slope of the dark matter density profile near the centres of dwarf galaxies measured from observations and simulations is called the core-cusp problem (e.g., Flores & Primack 1994; Moore 1994; Bullock & Boylan-Kolchin 2017; Lelli 2022).

There are at least three solutions to this problem that have been explored in the literature. First, dark matter could behave differently than assumed under the ΛCDM model. For example, if dark matter could interact with itself (so-called self-interacting dark matter or SIDM), the transfer of energy between dark matter particles would soften the density profiles, alleviating the core-cusp problem (e.g., Spergel & Steinhardt 2000; Vogelsberger et al. 2012; Peter et al. 2013; Fry et al. 2015; Elbert et al. 2015; Cyr-Racine et al. 2016; Vogelsberger et al. 2016; Kaplinghat et al. 2020; Leung et al. 2021).

* NSF Astronomy and Astrophysics Postdoctoral Fellow

† Contact e-mail: rebeccalevy@email.arizona.edu

¹ In some of the literature, the power-law slope is denoted as α , where $\alpha \equiv -\beta$. Here we use β throughout for consistency, such that $\rho(r) \propto r^{-\beta}$.

An important test for SIDM comes from galaxy clusters, where the upper-limit on the SIDM cross section is marginally consistent with the lower limit needed to alleviate the core-cusp problem, suggesting that such SIDM models are unlikely to be a solution to the core-cusp problem (Bullock & Boylan-Kolchin 2017). There are, however, a class of well-motivated, velocity-dependent SIDM scattering cross sections, which can reproduce the dark matter distributions and properties in both galaxy clusters and dwarf galaxies (e.g., Yoshida et al. 2000; Read et al. 2018; Valli & Yu 2018; Kaplinghat et al. 2020; Sagunski et al. 2021; Correa 2021). As pointed out by Bullock & Boylan-Kolchin (2017), warm dark matter models produce the same density distributions as CDM and are therefore not a solution to the core-cusp problem.

Another possibility is that systematic and/or measurement uncertainties in the rotation curve analysis may give rise to this tension. Rotation curves measured for some kinematic tracers are used to infer the circular velocity curve and hence the mass or density profiles². In the rotation curve analysis, a failure to properly account for non-circular motions can lead to measurements of cored profiles. It has been argued in the literature that triaxiality in the dark matter halo (as opposed to the often assumed spherical geometry) can induce non-circular motions in the gas disc (e.g., Simon et al. 2005; Hayashi & Navarro 2006; Read et al. 2016; Genina et al. 2018; Marasco et al. 2018; Oman et al. 2019; Santos-Santos et al. 2020; Jahn et al. 2021). If these non-circular motions are unaccounted for in the rotation curve analysis, they may lead to an underestimate of the true circular velocity and hence produce an apparent core-like dark matter profile. However, for these effects to completely explain the core-cusp problem, a clear explanation of why these non-circular motions only give the appearance of cores in low-mass galaxies is necessary. Moreover, non-circular motions can also lead to an over-prediction of the central circular velocity and instead produce an apparently *cuspier* dark matter density profiles. These non-circular motions can induce spurious diversity in rotation curve shapes (i.e. both steeper and shallower slopes) and must be accounted for to understand any underlying physical rotation curve diversity (e.g., Oman et al. 2015, 2019; Santos-Santos et al. 2018, 2020; Jahn et al. 2021). Therefore, while care should be taken to properly account for and measure non-circular motions in rotation curve analyses, such errors are unlikely to fully alleviate the core-cusp problem (e.g., Kaplinghat et al. 2020; Lelli 2022).

A possible solution within the Λ CDM paradigm is that baryonic physics and feedback impact the dark matter distribution in a galaxy. This feedback, especially from supernovae, can redistribute mass in a galaxy, reshaping the potential and hence the dark matter density distribution. This feedback will be most efficient in the centres of dwarf galaxies, where the dark matter density and star formation rate surface densities are highest. Numerical simulations, including feedback, find that the peak core-formation occurs in galaxies with stellar masses (M_{\star}) $\approx 10^{8-9} M_{\odot}$ (e.g., Navarro et al. 1996a; Governato et al. 2012; Pontzen & Governato 2014; Di Cintio et al. 2014; Chan et al. 2015; Tollet et al. 2016; Fitts et al. 2017; Hopkins et al. 2018; Lazar et al. 2020; Macciò et al. 2020). At smaller masses, the star formation rates are too low for the resulting stellar feedback to significantly alter the density distribution. At larger masses, the

gravitational potential is too deep for stellar feedback to significantly redistribute the dark matter into a core-like profile.

In this study, we build upon the set of observed inner dark matter density slopes using new observations of a sample of six galaxies from the Dwarf Galaxy Dark Matter (DGDGM) survey (Truong et al. 2017). Using new $^{12}\text{CO } J = 1 - 0$ observations from ALMA and *Spitzer* 4.5 μm data as tracers of the total potential and stellar component, we kinematically decompose the dark matter density profiles to measure the inner dark matter density slopes (β^*).

This work closely follows that of Relatores et al. (2019a,b, hereafter R19a and R19b), who measured β^* from another DGDGM survey sub-sample using H α observations to trace the total potential. β^* is defined as the slope of the dark matter density profile from 0.3–0.8 kpc, describing the shape of the dark matter density profile at small galactocentric radii. In contrast, β is the power-law exponent of the parametrized dark density profile, whether that be a pure power-law, a NFW profile, or another form. The β^* values derived by R19b agree with other CO data points from CARMA (Truong et al. 2017). Specifically, R19b find that one third of the inner slopes were consistent with the NFW profile, while the rest were more core-like than the NFW profile predicts.

From our sample of six dwarf galaxies, we find shallow cusp-like inner dark matter density distributions ($\langle\beta^*\rangle = 0.6$ with a standard deviation of ± 0.1 among the measurements). At first glance, our results broadly agree with predictions from the FIRE and NIHAO simulations, insofar as the dark matter profiles are shallower than predicted by a pure NFW profile in this stellar mass range of $10^{9.3-9.7} M_{\odot}$ (e.g., Tollet et al. 2016; Macciò et al. 2020; Lazar et al. 2020). However, when we calculate the inner dark matter density slope in the same way as these simulations (based on the virial radius, R_{vir}), we find that the slopes we measure are steeper than these simulations predict. These simulations find that cores can only be maintained through accretion, mergers, and/or outflows from stellar feedback which disturb the potential. We posit that these dwarfs are likely too massive for stellar feedback to effectively alter the dark matter distributions to be more core-like.

This paper is organized as follows. We describe the CO data used for this study and the data reduction in Section 2. Section 3 describes the method used to derive the CO rotation curves. The determination of the stellar components, decomposition of the dark matter density profiles, and measurement of β^* are presented in Section 4. Our results and robustness tests are described in Section 5. Implications of our results are discussed in Section 6. We summarize our conclusions in Section 7.

2 OBSERVATIONS AND DATA REDUCTION

The initial galaxy selection for the DGDGM survey is described by Truong et al. (2017), who observed these galaxies in $^{12}\text{CO } J = 1 - 0$ (CO) with the Combined Array For Millimeter-wave Astronomy (CARMA). Of the initially selected 26 galaxies, 14 were robustly detected in CO with CARMA. Of these, 13 were followed up with new and more sensitive CO observations using the Atacama Large Millimeter/submillimeter Array (ALMA) as part of project number 2015.1.00820.S (PI L. Blitz). These 13 galaxies were chosen to be bright and extended in the WISE 22 μm band (W4), to have substantial IRAS 100 μm flux, and to be far enough south to be visible to ALMA. These galaxies were observed in Band 3 in the C36-1 configuration with baselines ranging from 15 – 640 m and a maximum recoverable scale of $\approx 21''$ (~ 2 kpc for the mean distance to these galaxies of 21 Mpc). Mosaics of a few pointings were used

² In this paper, we use ‘rotation curve’ to refer to the measured rotation speed of some kinematic tracer. We use ‘(circular) velocity curve’ to refer to the velocity corresponding the mass distribution of some component of the galaxy (i.e., $V^2 = R \frac{\partial\Phi}{\partial R}$).

Table 1. CO Data Reduction and Imaging Parameters

Name	Beam (arcsec)	rms Noise (mJy beam ⁻¹)	(mK)	CASA Cal. Ver.
NGC1035*	2.90	4.2	46	4.5.1
NGC4310	2.40	4.1	65	4.5.3
NGC4451*	2.80	4.2	49	4.5.1
NGC4701	2.80	4.3	50	4.5.1
NGC5692*	2.85	4.7	53	4.5.1
NGC6106*	2.40	3.4	54	4.5.2

Galaxies marked with * overlap with [R19a](#) and [R19b](#). The FWHM of the synthesized, circularized Gaussian beam is given. The rms noise per 2 km s⁻¹ channel is reported for the cleaned cube for regions with no signal (SNR < 3) based on the peak intensity in mJy beam⁻¹ and mK. CASA Cal. Ver. lists the version of CASA used for calibration; all of the visibilities were imaged with CASA version 5.7.2-4.

for galaxies with large angular extents on the sky (e.g., NGC 1035 and NGC 6106). This configuration results in ~ 2'' (~ 200 pc for the mean distance to these galaxies) resolution that is well matched to the H α data from the Palomar Cosmic Web Imager presented by [R19a](#).

The visibilities were calibrated and flagged by the observatory using the Common Astronomy Software Application (CASA; [McMullin et al. 2007](#)) version listed in Table 1. The data were imaged using `tclean` in CASA version 5.7.2-4 with `deconvolver='hogbom'`, `specmode='cube'`, Briggs weighting with `robust=0.5`, and no `uv-taper`. The pixel (`cell`) sizes are listed in Table 1. The baseline was fit with a linear function (`nterms=2`) to account for any change in slope over the band. The imaging was performed on the three-dimensional RA-Dec-velocity images, where each spatial pixel (`spaxel`) contains a spectrum. These images were cleaned until the residuals were consistent with the root-mean-square (rms) noise levels given in Table 1. The final images all have a velocity resolution of 2 km s⁻¹, and we convolved the images to a circular beam, which is listed in Table 1. The rms noise per channel reported in Table 1 is calculated where the signal-to-noise ratio (SNR) < 3 based on the peak intensity maps (described in the following paragraph).

Moment maps (peak intensity, velocity, linewidth) were produced by fitting each pixel of the CO images with a Gaussian. Error maps are also produced based on the statistical uncertainties in the Gaussian fitting. Fits that do not converge are blanked. Isolated blanked pixels (i.e., where none of the neighbouring values is blanked) are replaced with the median value of the neighbours. Pixels in the CO intensity, velocity, and velocity dispersion maps with SNR < 3 based on the peak intensity and associated error maps are masked out. We impose a minimum velocity uncertainty of 6 km s⁻¹ to account for the random ISM motions (e.g., [R19a](#); [R19b](#)). This level also corresponds to ~1/3 of the typical CO linewidth. The CO peak intensity, velocity, and full-width-half-maximum (FWHM) linewidth maps are shown in Figure 1. All velocities presented in this work have been converted to the relativistic velocity frame (see e.g., Appendix A of [Levy et al. 2018](#) for details and conversions).

Of the 13 galaxies observed with ALMA, three galaxies (NGC 853, NGC 1012, NGC 4376) have insufficient signal to produce a velocity field even before our SNR mask is applied. Our SNR mask excludes three more galaxies (NGC 4150, NGC 4396, UGC 8516). Finally, we exclude NGC 4632. This galaxy is in a group with NGC 4666 (a large starburst galaxy), NGC 4668, and two other smaller dwarf galaxies ([Garcia 1993](#); [Walter et al. 2004](#)), though these ALMA observations only cover NGC 4632. The CO in NGC 4632 follows the spiral arms, with the northern spiral arm being much more prominent.

A single prominent spiral arm can be a sign of a past interaction (e.g., [Oh et al. 2008b](#)), which is possible for this galaxy given its known group membership. We therefore exclude this galaxy from the sample as the presence of other close, large galaxies and the hints of tidal interaction may affect the kinematics and dark matter halo of this system. Our final sample consists of six galaxies (NGC 1035, NGC 4310, NGC 4451, NGC 4701, NGC 5692, NGC 6106), shown in Figure 1 and listed in Table 1.

These ALMA observations cover antenna spacings from 15 – 640 m and filters out some of the flux on scales larger than $\approx 21''$. Lower-sensitivity CARMA data of these galaxies taken in the C, D, and E configurations (antenna spacings from 7.5 – 373 m) recover scales up to $\sim 40''$ ([Truong et al. 2017](#)). Importantly for our study, we are interested in the CO kinematics, as opposed to robust CO fluxes or molecular gas masses. As a test of the effects of the missing short spacings on the CO kinematics, we combined the ALMA and CARMA images using the `immerge` task in MIRIAD ([Sault et al. 1995](#)). We derived the velocity fields from these combined images in the same way as described above. The resulting combined velocity fields show no significant differences with the ALMA-only velocity fields. We therefore proceed using only the ALMA data in our analysis.

In addition to the CO data, we use *Spitzer* IRAC 4.5 μ m (Channel 2) maps from the Spitzer Survey of Stellar Structure in Galaxies (S4G; [Sheth et al. 2010](#); [Muñoz-Mateos et al. 2013](#); [Querejeta et al. 2015](#)) to trace the stars³. *Spitzer* IRAC data are not available for NGC 5692. We instead use *r*-band images from the 3 π Steradian Survey on the PAN-STARRS1 (PS1) telescope ([Chambers et al. 2016](#))⁴. PS1 *r*-band and *Spitzer* 4.5 μ m images are shown for these galaxies in Figure 1.

Distances to these galaxies are taken from two sources. Three of our galaxies have Tully-Fisher distances reported by [Tully et al. \(2013\)](#). For the other three, we use the distances from the `modbest` column in the HyperLEDA catalogue ([Makarov et al. 2014](#))⁵. These distances (and their uncertainties) are reported in Table 2.

3 DERIVATION OF CO ROTATION CURVES

We derive the CO rotation curves using a first order harmonic decomposition:

$$V(r) = V_{\text{rot}}(r) \cos \phi \sin i + V_{\text{rad}}(r) \sin \phi \sin i + \Delta V_{\text{sys}}(r) \quad (1)$$

which fits for the rotation (V_{rot}), radial (V_{rad}), and systemic (ΔV_{sys}) components, where r is the galactocentric radius, ϕ is the azimuthal angle in the plane of the disk, and i is the inclination and is assumed the same for all rings (e.g., [Begeman 1989](#)). Before fitting, the central systemic velocity (V_{sys}) is subtracted from the map, such that the fitted systemic component (ΔV_{sys}) describes the deviation from this value. We extract the rotation velocities in concentric rings using a new Python implementation⁶ of the original MATLAB code developed by [Bolatto et al. \(2002\)](#) and used by [Simon et al. \(2003, 2005\)](#). [Levy et al. \(2018\)](#) modified the ring spacing algorithm so that

³ These images were downloaded directly from the NASA/IPAC Infrared Science Archive: <https://irsa.ipac.caltech.edu>.

⁴ These images were downloaded directly from the PS1 Image Cutout Server: <https://ps1images.stsci.edu/cgi-bin/ps1cutouts>.

⁵ <http://leda.univ-lyon1.fr/>

⁶ The Python implementation of the rotation curve fitting code is publicly available at <https://github.com/rclevy/RotationCurveTiltedRings>.

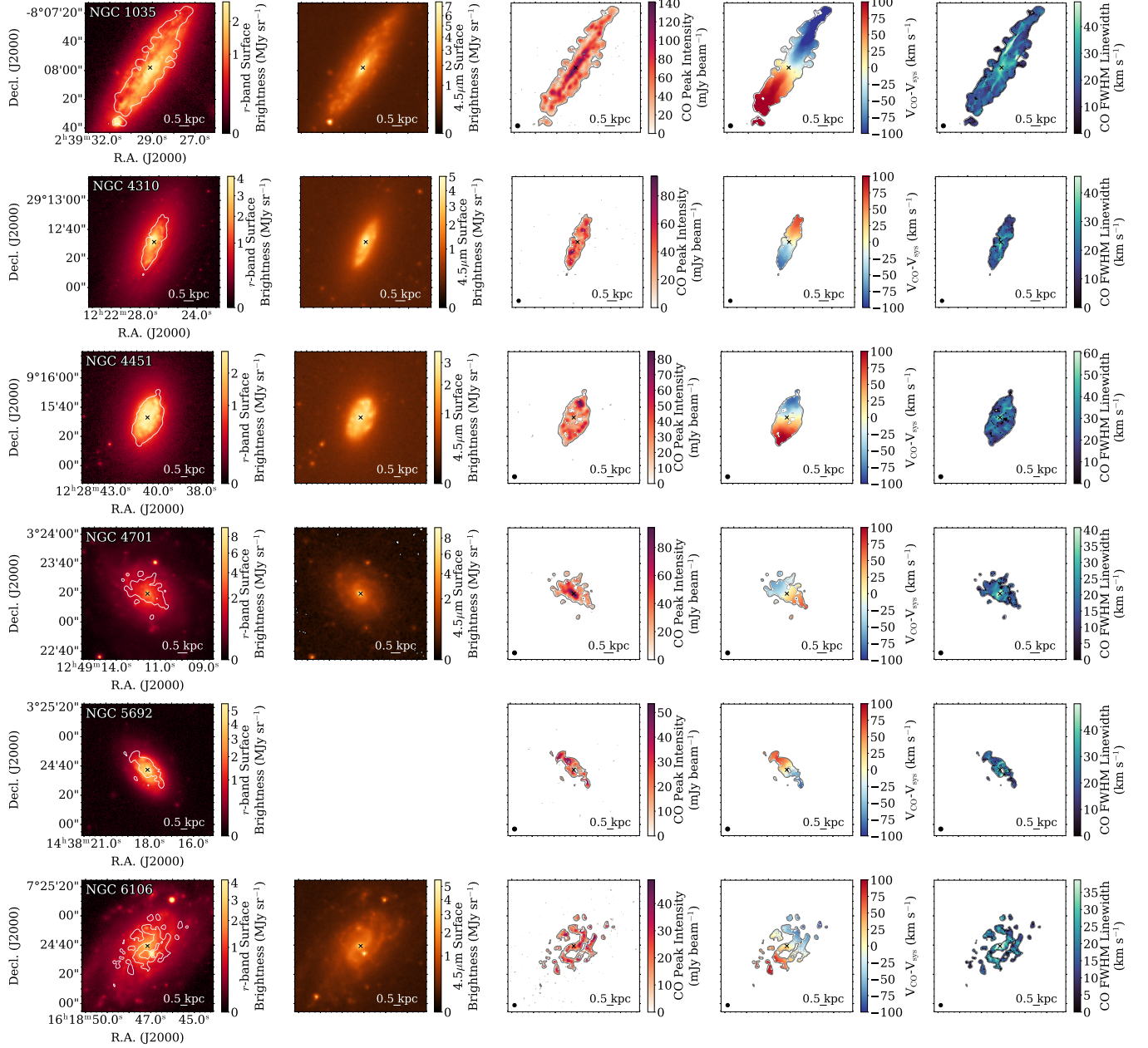


Figure 1. The six galaxies studied here, showing (from left to right) their PS1 r -band images, *Spitzer* $4.5 \mu\text{m}$ images, the CO peak intensity, the CO velocity, and the CO FWHM linewidth. There is no *Spitzer* image for NGC 5692. Each image is cropped to $1.5'$ on a side. The crosses show the location of the kinematic centre (Table 2). The white or grey contours show $\text{SNR} = 3$ based on the CO peak intensity. The CO maps are masked to this level. The black ellipses in the lower left corners of the CO images show the FWHM beam sizes.

rings are spaced in half-beam-width increments or contain at least 30 pixels per ring, whichever is larger.

The initial values for the kinematic parameters (centre, position angle, inclination, systemic velocity) were taken from [Truong et al. \(2017\)](#), but were adjusted by hand as needed. We modify the centre position of each galaxy to minimize the ΔV_{sys} component at small radii, as offsets from the correct centre induce sharp deviations from zero in this component very near the centre. We then adjust the systemic velocity value (V_{sys}) such that $\Delta V_{\text{sys}} \approx 0$. The position angle (PA) takes values between 0° and 360° , where $\text{PA} = 0^\circ$ indicates that the receding side is oriented north, and increases counterclockwise

(east of north). The PA is modified such that $V_{\text{rad}} \approx 0$ throughout the galaxy, as an incorrect PA induces a constant offset in V_{rad} . For galaxies where there are radial trends in V_{rad} , the PA is adjusted to minimize V_{rad} in the outer regions of the galaxy. In galaxy centres, there may be non-circular motions due to bars and/or inflows, and the V_{rad} component is sensitive to these non-circular motions. Moreover, as briefly mentioned in Section 1, improperly accounting for non-circular motions can affect the derived circular velocity curve and hence the inner slope of the dark matter density profile (e.g., [Marasco et al. 2018](#); [Oman et al. 2019](#); [Santos-Santos et al. 2020](#)). The inclination was adjusted based on the harmonic fits in

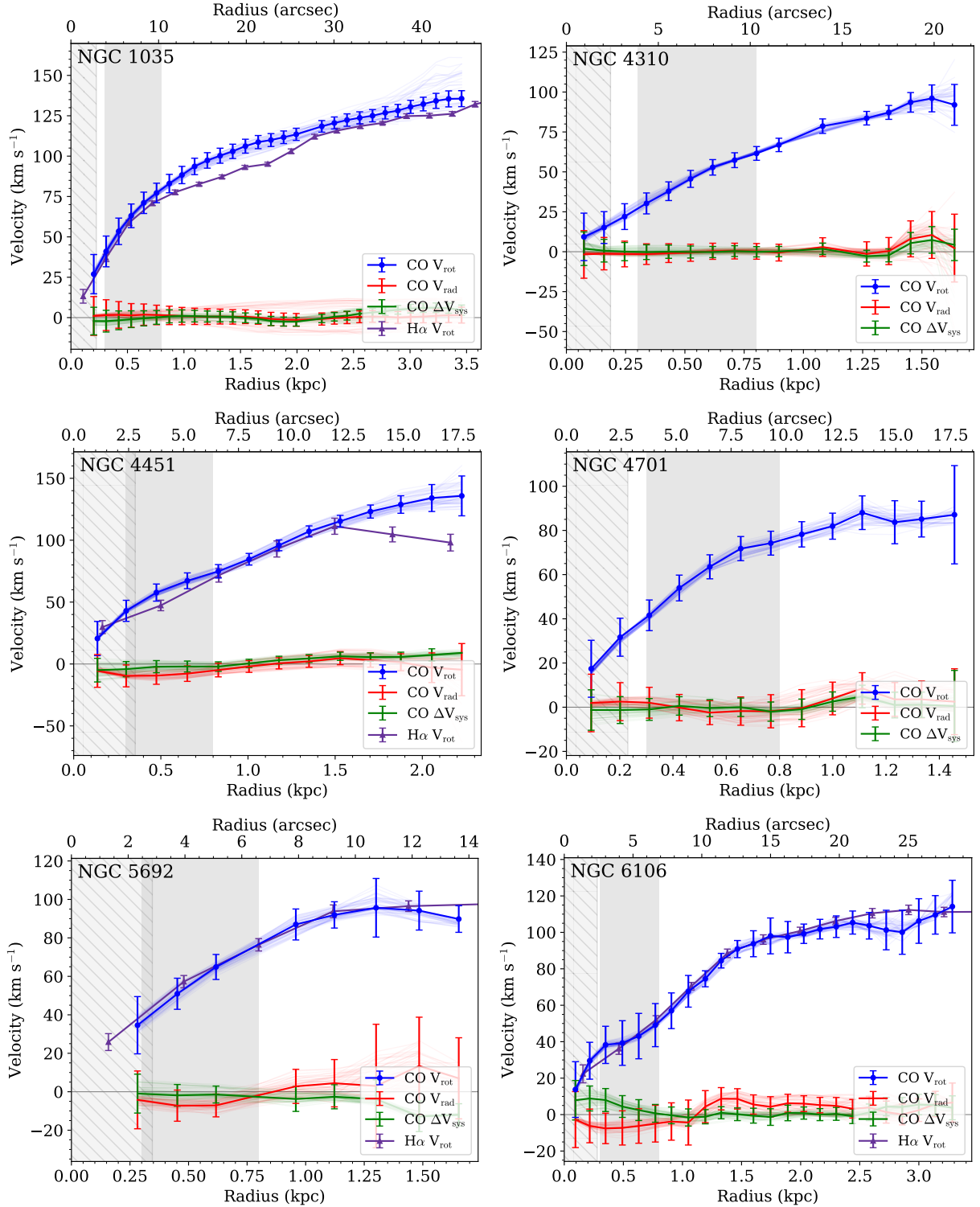


Figure 2. CO rotation curves for the six galaxies studied here using the parameters in Table 2. The fits use a first order harmonic decomposition (Equation 1), where V_{rot} is shown in blue, V_{rad} in red, and ΔV_{sys} in green. The thick lines show the best fitting values for each component. The uncertainties shown by the error bars reflect the statistical fitting uncertainties in each ring. The thin translucent lines show the Monte Carlo trials, varying the centre position, PA, and inclination. See Section 3 for details. The grey hatched region shows twice the beam HWHM, indicating radii over which the CO measurements may be most affected by beam smearing. The solid grey region shows the range of over which β^* is calculated. The purple curves show the H α rotation curve derived by R19b, where available. The error bars on the H α rotation curves reflect the statistical fitting errors. In general, the CO and H α rotation curves agree well; see Section 3.2 for notes on individual galaxies.

Table 2. Parameters from Rotation Curve Fitting

Name	R.A. (J2000 hours)	Decl. (J2000 deg)	Distance (Mpc)	V_{sys} (km s^{-1})	PA (deg)	Inc (deg)	R_{max} (kpc)	$\log M_{\text{dyn}}(R_{\text{max}})$ ($\log M_{\odot}$)	σ_V (km s^{-1})
NGC1035	2 ^h 39 ^m 29.1 ^s	−8°07′58.2″	15.9 ± 3.2 (a)	1224	144	79	2.9	10.0 ± 0.1	20.6 ± 7.8
NGC4310	12 ^h 22 ^m 26.3 ^s	+29°12′31.1″	16.1 ± 7.4 (b)	927	335	71	1.6	9.5 ± 0.1	19.0 ± 5.8
NGC4451	12 ^h 28 ^m 40.5 ^s	+9°15′32.5″	25.9 ± 5.2 (a)	849	178	49	2.2	10.0 ± 0.1	25.3 ± 7.8
NGC4701	12 ^h 49 ^m 11.6 ^s	+3°23′19.0″	16.7 ± 2.7 (b)	725	230	49	1.5	9.4 ± 0.1	17.1 ± 6.4
NGC5692	14 ^h 38 ^m 18.1 ^s	+3°24′37.1″	25.4 ± 7.4 (b)	1605	36	53	1.7	9.5 ± 0.1	21.6 ± 8.4
NGC6106	16 ^h 18 ^m 47.2 ^s	+7°24′39.3″	24.3 ± 4.9 (a)	1465	143	59	3.3	10.0 ± 0.1	18.1 ± 8.7

R.A. and Decl. list the best fit center. The distances and uncertainties are from (a) Tully et al. (2013) where available or (b) the modbest column in HyperLEDA otherwise (see Section 2). V_{sys} is in the relativistic velocity frame. The PA is measured E of N to the receding side of the major axis. $M_{\text{dyn}}(R_{\text{max}})$ is the dynamical mass measured from the CO rotation curve at radius R_{max} . σ_V is the median FWHM velocity dispersion, uncorrected for beam smearing; the uncertainty is the standard deviation.

each ring, where an incorrect inclination can result in flat-topped or peaked harmonic models whose shapes do not match the data. The PA and inclination are each fixed to a single value at all radii. Our CO rotation curves are shown in Figure 2, and the final values of the kinematic parameters are listed in Table 2. We show the residual velocity maps (the difference between the CO velocity field and our best-fitting harmonic decomposition) in Figure A1 in Appendix A, which were used as additional checks on our geometric parameters (e.g., van der Kruit & Allen 1978).

We determine the uncertainties on the rotation curves as follows. First, we calculate the statistical fitting uncertainty in each annulus. This includes the effect of correlations between pixels due to the Gaussian beam. These uncertainties are shown as the error bars in Figure 2. Next, we account for the systematic uncertainties related to the input geometric parameters using a Monte Carlo method. In each realisation, the centre position is allowed to vary uniformly by $\pm 0.4''$, the position angle by $\pm 5^\circ$, and inclination by $\pm 4^\circ$ from the best-fitting kinematic parameters in Table 2. These values come from the median differences in the centre position, PA, and inclination used here compared to those kinematically derived by R19a. We use 50 trials. The fits from each of these trials are shown as the faint thin lines in Figure 2 and their scatter reflects the systematic uncertainties due to the input geometric parameters. At most radii, uncertainties from the fitting in each ring dominates the total uncertainty of the rotation curves. However, systematic uncertainties from changing the geometric parameters can dominate at large radii.

The central regions of the rotation curve are, to some degree, affected by beam smearing (e.g., Warner et al. 1973; Bosma 1978; Begeman 1987; Teuben 2002; Leung et al. 2018). Beam smearing has the effect of artificially lowering the rotation velocity and increasing the velocity dispersion. This effect is worst in the central regions where the rotation curve rises sharply and for highly inclined systems (e.g., Leung et al. 2018). For our sample, the effect of beam smearing can be most clearly seen in the linewidth map of NGC 1035 (upper right-most panel of Figure 1), which shows the characteristic \times pattern induced by this effect (e.g., Teuben 2002). For this analysis, we do not correct for beam smearing. In Figure 2, the grey hatched regions show twice the beam half-width-half-maximum (HWHM), indicating the radii most affected by beam smearing. As discussed in the following section, the inner slope of the dark matter density profile is calculated from 0.3–0.8 kpc. There is only minimal overlap between this radius range and where the effects of beam smearing will be most apparent, so we conclude that beam smearing does not significantly affect the results presented here.

In order to use CO as the tracer of the total galaxy potential (i.e., to use the CO rotation curve as the circular velocity curve of the

total galaxy potential), the CO must be dynamically cold. To verify this, we find the median CO velocity dispersion for each galaxy (uncorrected for beam smearing), which are listed in Table 2. The velocity dispersions are quite low and the galaxies have $\frac{V_{\text{rot}}}{\sigma_V} > 4$, which both indicate that the CO is dynamically cold in these galaxies. We calculate the dynamical mass (M_{dyn}) at the measured maximum radius of our CO rotation curve (R_{max}). Our measurement of M_{dyn} is a lower limit on the true dynamical mass of these galaxies, especially since the rotation curves generally continue to rise as they approach R_{max} .

3.1 Correlations between points and uncertainties in the CO rotation curves

As we will describe in Section 4.3, the method we use to decompose the dark matter density profiles assumes that the points in the CO rotation curves are independent and that the uncertainties are Gaussian and independent as well.

The beam (i.e. the point-spread function, PSF) of the CO observations is a Gaussian, and the chosen pixel size of the images oversamples the beam by a factor of ~ 6 . This means that no pixel in the CO map is perfectly independent from any other pixel. Therefore, even though the rings used to derive the rotation curves do not overlap, pixels in those rings are not perfectly independent. The choice to space the rings at half-beam FWHM intervals (i.e., Nyquist sampling) mitigates correlations between rings. As a more direct test, we increased the pixel size of the CO velocity fields to decrease this oversampling and repeated the derivation of the CO rotation curves; the resulting CO rotation curves and uncertainties were essentially unchanged from the original versions. Therefore, correlation between points in the CO rotation curve due to the beam is relatively minor, and we proceed with the decomposition as if they were perfectly independent (Section 4.3).

The Monte Carlo sampling we performed over the geometric parameters means that the systematic uncertainties from this method are highly correlated from ring to ring. The PA and inclination drive these correlations: as the PA and/or inclination are changed, the entire rotation curve shifts (primarily) vertically, as shown by the thin faint lines in Figure 2. These uncertainties from the Monte Carlo sampling are, in general, smaller than the uncertainties from the fitting itself, which reflect the statistical fitting uncertainty in each ring. We use the statistical fitting uncertainty as the uncertainty on the measured circular velocity curves (of the total galaxy potential) in the decomposition as described in Section 4.3. We proceed assuming that the uncertainties in the rotation curves are Gaussian and independent between points. We include the effects of uncertainties in the PA

and inclination in the decomposition directly, as we will describe in Section 4.3.

3.2 Notes on individual galaxies

Here, we briefly provide notes on each galaxy in this sample. All morphological information is taken from the HyperLEDA catalogue.

NGC 1035 — This spiral galaxy is the most highly inclined of the subsample. Its CO V_{rot} lies systematically above the H α V_{rot} derived by R19a, but the shapes of the rotation curves agree well. The shape of the rotation curve is most important for determining the slope of the dark matter density profile. The amplitude depends on the inclination. For this galaxy, we use a somewhat higher inclination than R19a (79° compared to their 72°), but this does not completely explain the offsets between the CO and H α rotation curves.

NGC 4310 — This galaxy is classified as intermediate between a lenticular and spiral galaxy. From the optical and $4.5 \mu\text{m}$ data (Figure 1), there appears to be a dust lane. The CO traces the extent of the bright optical and NIR emission. Kinematically, this is a very well-behaved galaxy, with only a small ΔV_{sys} component in the centre.

NGC 4451 — This spiral galaxy was also observed in H α , though its mass model was graded as low-quality (R19b). There is a significant offset between the CO and H α rotation velocities at large radii and the H α rotation velocity is slightly lower than that of the CO overall, which may be due to irregular ionized gas kinematics in the outer regions of this galaxy. In the inner regions, the slopes of the rotation curves agree well. We use a slightly larger inclination compared to R19a (49° compared to their 45.1°), but this does not completely explain the small offset between the CO and H α rotation curves at radii less than 1.5 kpc.

NGC 4701 — This spiral galaxy shows no evidence for a bar, though the spiral arms are prominent and strong towards the centre. CO is mainly detected on the blueshifted side of the galaxy. This is not due to a tuning error, but rather due to less signal on the redshifted side of the galaxy.

NGC 5692 — This spiral galaxy has no evidence for a bar. The agreement between the rotation curves derived from the CO and H α is better than 3 km s^{-1} on average. We use nearly the same inclination as R19a (53° compared to their 52.4°). There is no *Spitzer* IRAC data available for this galaxy, so r -band data are used to measure the stellar components instead.

NGC 6106 — This spiral galaxy has strong spiral arms, and the CO detections are concentrated in the spiral arms. There is no reported bar, though the spiral arms in the centre may contribute to the non-zero radial velocity component seen in the CO rotation curve fits. This is the largest galaxy in the sample, in terms of angular and physical CO extent. We use a slightly higher inclination of 59° compared to R19a who found 53.4° . The agreement between the CO and H α rotation curves is excellent, though there appears to be a slight increase in the CO velocity at very small radii that is not seen in the H α , though this may be explained by the finer radial sampling of the CO data.

4 DETERMINING THE DARK MATTER DENSITY PROFILES

Our method for decomposing the contributions of the various tracers to the total circular velocity curve follows that of R19b. To summarize, we can determine the dark matter velocity curve, $V_{\text{DM}}(r)$, knowing the circular velocity curve of the total potential, $V_{\text{tot}}(r)$, and

the contributions from the stars, $V_{\star}(r)$, atomic gas, $V_{\text{atomic}}(r)$, and molecular gas, $V_{\text{mol}}(r)$:

$$V_{\text{tot}}(r)^2 = V_{\text{DM}}(r)^2 + V_{\star}(r)^2 + V_{\text{atomic}}(r)^2 + V_{\text{mol}}(r)^2. \quad (2)$$

$V_{\star}(r)$ is calculated from *Spitzer* $4.5 \mu\text{m}$ or r -band photometric data (Section 4.1). The contributions of the atomic and molecular gas components are negligible compared to the stars and dark matter (Section 4.2). We include these components when available from R19b, otherwise their contributions are set to zero. We use the CO rotation curves as our measurement of $V_{\text{tot}}(r)$. As described in Section 3, the measured CO velocity dispersions are low (Table 2), even without a correction for beam smearing, meaning that the CO is a robust, dynamically cold tracer of the total potential.

Therefore, having measured the total potential, the stellar component, and the contributions from the atomic and molecular components where available, we can solve for the contribution from the dark matter. As we describe in Section 4.3, we use a forward-modelling Markov Chain Monte Carlo (MCMC) approach to measure the dark matter component. From the best-fitting dark matter density profile, we compute β^* , the slope of the dark matter density profile from $0.3 - 0.8 \text{ kpc}$.

4.1 Stellar mass and velocity profiles

We derive the stellar circular velocity curves starting from the *Spitzer* IRAC $4.5 \mu\text{m}$ maps (Figure 1). As discussed by R19a and R19b, the $4.5 \mu\text{m}$ data are preferred since they more closely trace the stellar mass distribution than the r -band data. Using the geometric parameters listed in Table 2, the $4.5 \mu\text{m}$ maps were divided into annuli centred on the centre of the galaxy. For radii that overlap with the CO rotation curves, the radial binning matches that of the CO. For radii beyond the CO extent, the annuli are 5 pixels wide and extend out to a radius $R_{\text{max},\star}$ (listed in Table 3). The cumulative stellar mass profiles do not continue to rise substantially at $R_{\text{max},\star}$, so stellar masses calculated at this radius encompass nearly all of the stellar mass of the galaxies. The surface brightness was summed in each annulus and converted to a luminosity. To convert to solar luminosities, we find the luminosity of the Sun at $4.5 \mu\text{m}$ using the IRAC Channel 2 zero-point (0 Vega mag = 179.7 Jy; Reach et al. 2005) and the absolute magnitude of the Sun at $4.5 \mu\text{m}$ ($M_{\odot}^{4.5} = 3.27 \text{ Vega mag}$; Oh et al. 2008a). This yields $L_{\nu,\odot}^{4.5} = 1.06 \times 10^{18} \text{ erg s}^{-1} \text{ Hz}^{-1}$ or $\nu L_{\nu,\odot}^{4.5} = 7.05 \times 10^{31} \text{ erg s}^{-1} = 0.018 L_{\odot}$. To convert to mass, we assume a constant mass-to-light ratio (Y_{\star}) from stellar population synthesis models reported by R19b (see their Table 1). For those galaxies that do not overlap with R19b's sample, we take their average $Y_{\star} = 0.21 \pm 0.04$. We report the Y_{\star} values used in this work in Table 3.

Spitzer IRAC $4.5 \mu\text{m}$ data are not available for NGC 5692. Like R19b, we instead use r -band images from PS1 (Figure 1) and employ the same method as described above to calculate the surface brightness profiles. The filters on PS1 are quite similar to the corresponding Sloan Digital Sky Survey (SDSS) filters (Tonry et al. 2012). The absolute magnitude of the Sun is 4.65 AB magnitudes in the SDSS r -band (Willmer 2018), and the effective central wavelength of the PS1 r -band filter is 617 nm (Tonry et al. 2012). This yields $L_{\nu,\odot}^r = 5.99 \times 10^{18} \text{ erg s}^{-1} \text{ Hz}^{-1}$ or $\nu L_{\nu,\odot}^r = 2.91 \times 10^{33} \text{ erg s}^{-1} = 0.746 L_{\odot}$. To convert to mass, we use the r -band Y_{\star} from stellar population synthesis models derived by R19b ($Y_{\star} = 0.83 \pm 0.15$; see their Table 1 and our Table 3).

We use NEMO (Teuben 1995) to determine the stellar velocity component from the extracted stellar surface brightness profiles. We

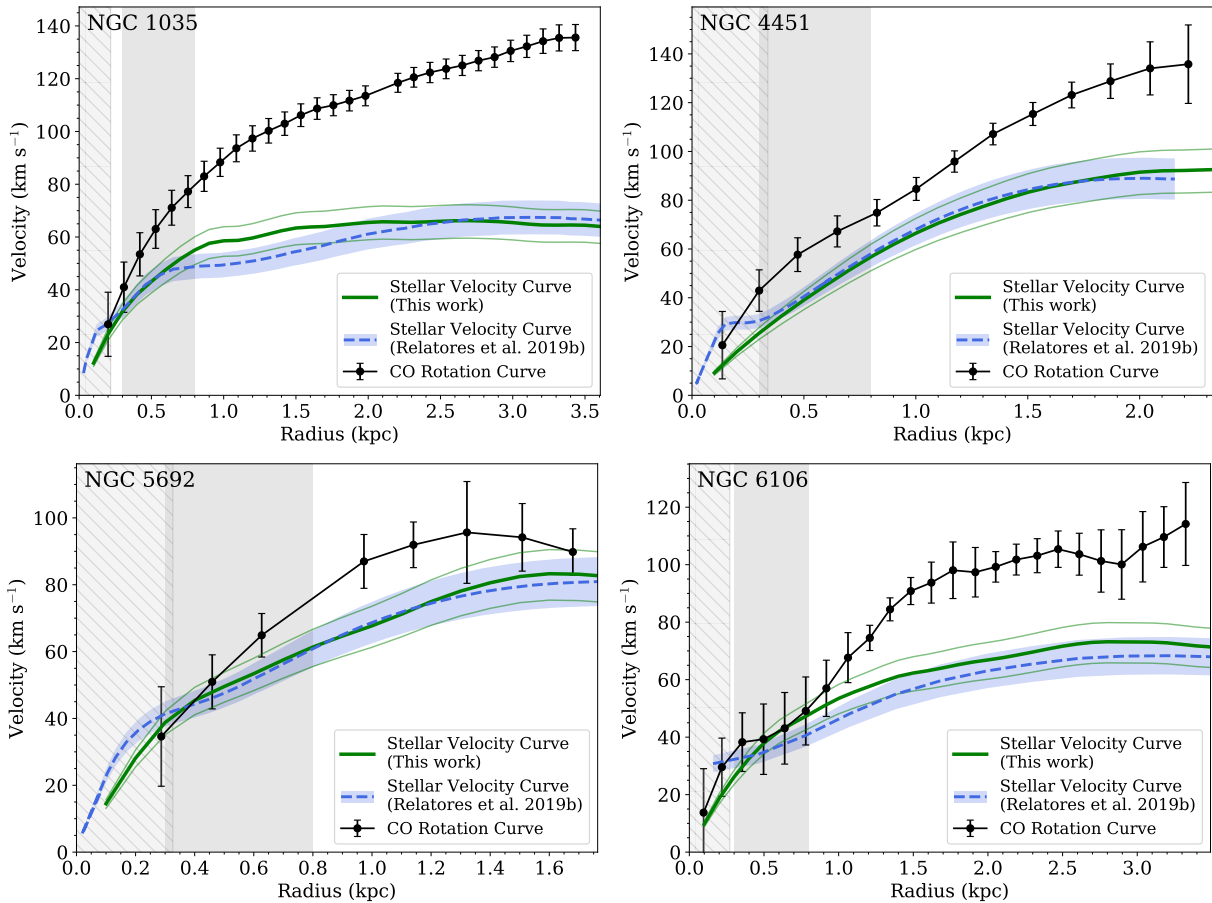


Figure 3. A comparison of the stellar velocity curves derived as described in Section 4.1 (green) compared to those derived by R19b (blue dashed). The thin green curves show the effect of changing the Y_{\star} within the range listed in Table 3, whereas the thick green curve shows the fiducial value of Y_{\star} . We also show the CO rotation curves (black) which trace the total potential. In general, the agreement between these methods is good, especially in the radial regime where β^* is calculated (grey shaded region). The grey hatched region shows twice the CO beam HWHM, indicating the central regions in which the CO rotation velocities may be affected by beam smearing.

assume that the stars are in a thin disk. In reality, the stars are likely in an oblate spheroid distribution. However, the axis ratios of stellar distributions tend to be small (e.g., Kregel et al. 2002), and all of the galaxies used here are classified as spirals. For their modelling, R19b assume an oblate spheroid with $c/a = 0.14$ motivated by observations. Where possible, we compare our derived stellar circular velocity curves (assuming a thin disk) to those derived by R19b (Figure 3). In general, the agreement (both in terms of shape and amplitude) are good, especially over the range of radii where β^* is calculated. The stellar circular velocity curves derived by R19b tend to be higher than ours in the centres, which may be due to our coarser binning. The total stellar masses of the galaxies in our sample (listed in Table 3) agree with those measured by R19b within the uncertainties, where available.

If the stellar velocity component is higher than the circular velocity based on the CO rotation curve, we fix V_{\star} at those radii to a maximal disk (i.e. where the stellar component accounts for the total potential). We increase the uncertainty on the stellar component in these bins by adding the velocity difference to the existing uncertainty in quadrature. The first five bins in NGC 4701 and the first bin in NGC 5692 are affected by this change.

4.1.1 Correlations between points in the stellar rotation curves

As we will describe in Section 4.3, the points in the stellar rotation curve are assumed to be independent, and the uncertainties are assumed to be Gaussian and independent as well. Similar to the CO maps (Section 3.1), the PSF of the *Spitzer* 4.5 μ m observations induces some correlation between pixels in the maps. The *Spitzer* PSF at 4.5 μ m has a FWHM of 1.6'' (Sheth et al. 2010), about half that of the Gaussian CO beams (Table 1). Where the decomposition can be performed, the stellar rotation curve rings have the same spacing as the CO. Therefore, points in the stellar rotation curves are even less correlated than in the case of the CO rotation curves. We proceed with the decomposition as if they were perfectly independent (Section 4.3).

4.2 Atomic and molecular gas components

For the four galaxies that overlap with R19b, we also include contributions from the atomic and molecular gas in the decomposition. We refer the reader to that paper for a detailed discussion of how these components were measured. We do not include uncertainties on the atomic and molecular components for this analysis (nor are they given by R19b). For the other two galaxies, however, we assume that these components are a negligible contribution to the mass. As we

will discuss in Section 5.1, including or excluding these components does not affect the final results.

4.3 Decomposing the dark matter component

Knowing the contributions from the stars (and atomic and molecular gas, if available) and the total potential, we can derive the dark matter density profile, following Equation 2. We take a forward-modelling approach, generating trials of the dark matter density profile and minimizing the difference between the model total circular velocity curve and that observed from the CO as described below.

We assume that the dark matter density profile is described by a generalised Navarro-Frenk-White (gNFW; Zhao 1996) profile of the form

$$\rho_{\text{DM}}(r) = \frac{\rho_o}{(r/r_s)^\beta (1+r/r_s)^{3-\beta}} \quad (3)$$

where r_s is the scale radius, ρ_o is the characteristic density, and β sets the slope as $r \rightarrow 0$. Setting $\beta = 1$ recovers the original NFW profile.

We transform this density profile into its corresponding velocity curve, $V_{\text{DM}}(r)$, where

$$V(r)^2 = \frac{4\pi G}{r} \int_0^r \tau^2 \rho(\tau) d\tau. \quad (4)$$

We use an affine invariant MCMC method (EMCEE; Foreman-Mackey et al. 2013) to draw samples of ρ_o , r_s , and β (as well as Y_\star , PA, and inclination as described below) to generate trials of the dark matter density and associated velocity curve (Equations 3 and 4). The uniform priors on ρ_o , r_s , and β are set such that $0 < \frac{\rho_o}{M_\odot \text{pc}^{-3}} < 1.0$, $0 < \frac{r_s}{\text{kpc}} < 10$, and $-2.5 < \beta < 2.5$.

As described in Section 4.1.1, Y_\star is included as a parameter in the model which scales the stellar velocity curve as $Y_\star^{\frac{1}{2}}$. Therefore, $V_\star(r|Y_\star)$ explicitly. The uniform priors on Y_\star are given by the ranges in Table 3.

There are known degeneracies between the geometric parameters and properties of the dark matter halo (for example, between the halo mass and inclination; e.g., Maller et al. 1997; Oguri et al. 2005; Read et al. 2016). We therefore include the PA and inclination as (nuisance) parameters to be fit in the MCMC. Rather than re-fitting the rotation curve at each step in the MCMC, which would be computationally expensive, we first generate a grid of rotation curves by varying the PA and inclination. We allow the priors on the PA (inclination) to vary uniformly by $\pm 5^\circ$ ($\pm 4^\circ$) from the best-fitting value in steps of 1° , which is based on the range from the Monte Carlo analysis discussed in Section 3. We use the grid of rotation curves as a lookup table, choosing the CO rotation curve with the nearest PA and inclination to each MCMC trial, acknowledging that there is some (small) error introduced by discretising the PA and inclination in this way.

Our likelihood function is given by

$$\ln \mathcal{L} = -\frac{1}{2} \sum_i \frac{(V_{\text{CO},i} - V_{\text{tot},i})^2}{\sigma_{\text{CO},i}^2}. \quad (5)$$

where V_{tot} is our model of the total circular velocity curve of the galaxy given by Equation 2. As described in Section 3.1, σ_{CO} are the uncertainties directly from the harmonic decomposition fitting and reflect the statistical fitting uncertainty in each ring (see Section 3.1 for more details).

We initialize the MCMC with $\rho_o = 0.5 M_\odot \text{pc}^{-3}$, r_s equivalent to the maximum radius in the CO rotation curve, $\beta = 0.5$, the PA and inclination given in Table 2, and Y_\star given in Table 3. We use

300 walkers for 300 steps. By examining the chains, the MCMC has forgotten the initial conditions after 50 steps. To be conservative, we discard the initial 100 steps.

The best-fitting parameters are given by the median of the marginalized posterior parameter distributions. The uncertainties are given by the 16th and 84th percentiles, which is equivalent to $1-\sigma$ for a Gaussian distribution. The best-fitting values of ρ_o , r_s , β , Y_\star , PA, and inclination are given in Table B1, and the posterior distributions of ρ_o , r_s , and β are shown in Figure B1 in Appendix B. The fitted values of Y_\star , PA, and inclination are consistent well within the uncertainties with the fiducial values in Tables 2 and 3. The best-fitting velocity decompositions are shown in Figure 4.

4.4 Measuring the inner slope of the dark matter density profile

We are interested in the inner slope of the dark matter density profile. Following R19b, we define ‘inner’ as radii from 0.3 – 0.8 kpc and denote the slope in this radial range as β^* :

$$\beta^* \equiv -\frac{\log\left(\frac{\rho_{\text{DM}}(0.8 \text{ kpc})}{\rho_{\text{DM}}(0.3 \text{ kpc})}\right)}{\log\left(\frac{0.8 \text{ kpc}}{0.3 \text{ kpc}}\right)}. \quad (6)$$

We calculate β^* at each step in the MCMC chain. The best-fitting value of β^* is given by the median of the distribution and the quoted uncertainties are the 16th and 84th percentiles (upper right corner panels of Figure B1). Our final values of β^* and uncertainties are reported in Table 3.

As shown in Table 2, the uncertainties on the distances to these galaxies are > 20 per cent. These uncertainties affect the conversion from angular to physical distance and hence the radial range over which β^* is measured. As a test of how the distance uncertainties affect our measurement of β^* , we re-scale the velocity curve radii and re-calculate β^* assuming the minimum and maximum distances to the galaxy. We find these values of β^* are consistent with the fiducial values within the uncertainties. Therefore, though the uncertainties in the galaxy distances has some effect, it is not the dominate source of uncertainty on our measurement of β^* .

For NGC 4701 (and the innermost point of NGC 5692), we fix the stellar velocity curve to a maximal disk where the observed stellar velocity is larger than the CO rotation curve (see Section 4.1). As a test, we relax the maximal disk assumption for NGC 4701 and re-fit β^* . Though we find a slightly shallower slope ($\beta^* = 0.1^{+0.6}_{-0.5}$), it is consistent with the slope measured for a maximal disk ($\beta^* = 0.4^{+0.8}_{-0.3}$) well within the uncertainties.

Rather than our definition of β^* in Equation 6, the inner slope of the dark matter density profile is often, especially in simulation-based analyses, defined between 1 – 2 per cent of the virial radius (R_{vir}). It is often convenient to define $R_{\text{vir}} \equiv R_{200}$, where R_{200} is the radius at which the density is 200 times the critical density (ρ_{crit} ; e.g., Bullock & Boylan-Kolchin 2017). We refer to this density as $\rho_{200} (\equiv 200\rho_{\text{crit}})$. The mass enclosed within R_{200} is M_{200} . Assuming a local Universe value of $H_0 = 73.2 \text{ km s}^{-1} \text{ Mpc}^{-1}$ (Riess et al. 2021; Di Valentino et al. 2021) yields $\rho_{\text{crit}} = 148.7 M_\odot \text{ kpc}^{-3}$. We extrapolate our best-fitting density profile for the total potential to estimate $R_{\text{vir}} (\equiv R_{200})$ and M_{200} (Table 3). Given the uncertainties on the total density profile, we estimate the uncertainty on R_{vir} and hence M_{200} . We find that 0.3 – 0.8 kpc corresponds to 0.3 – 1.6 per cent of R_{vir} for these galaxies. Said another way, 1 – 2 per cent of R_{vir} corresponds to 0.6 – 1.8 kpc for these galaxies (Table 3). Accounting for the uncertainties on R_{vir} , the 1 – 2 per cent of R_{vir} spans a range of 0.1 – 5.0 kpc. Therefore, our definition of β^* tends to probe

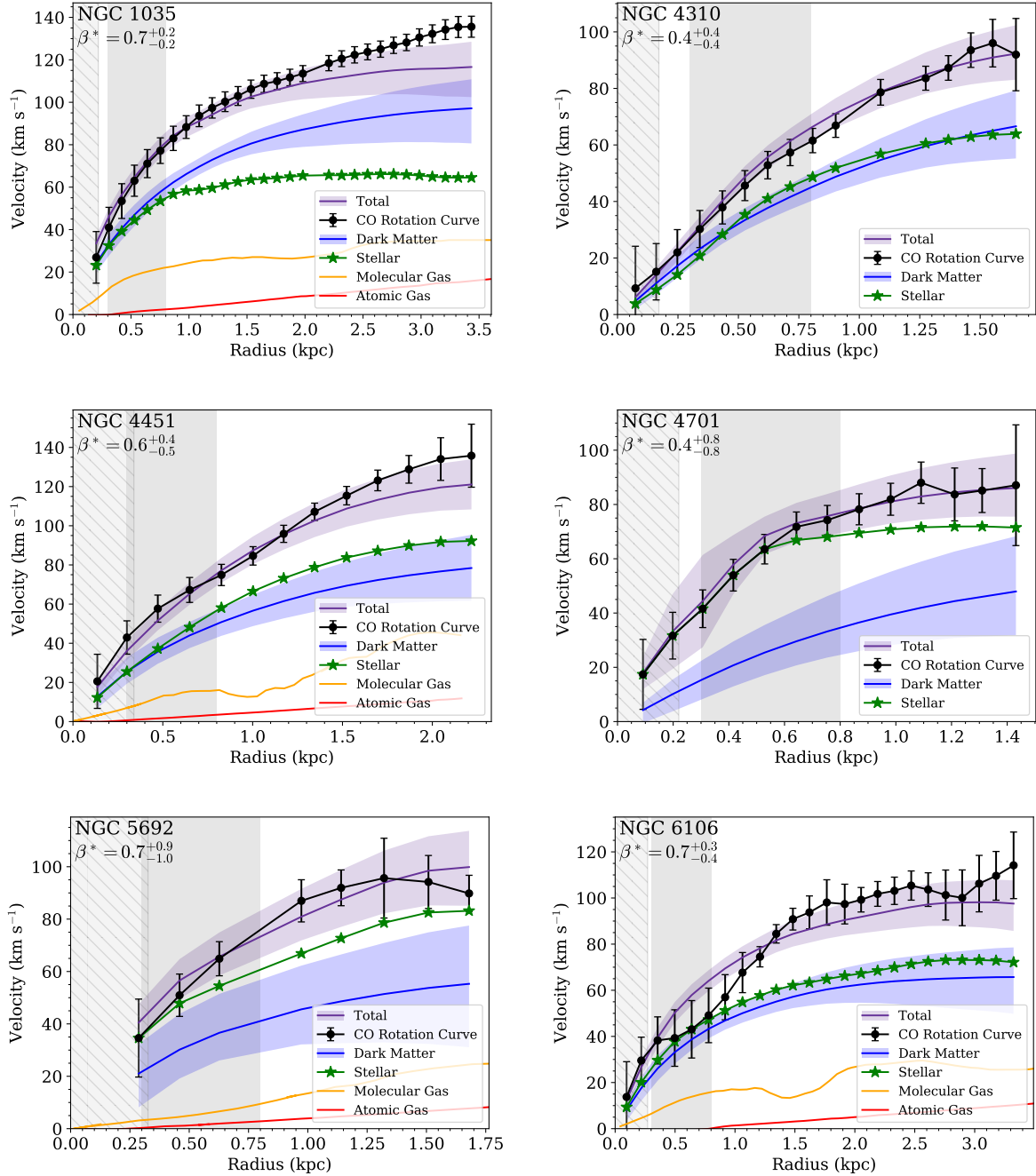


Figure 4. The results of the density profile decomposition, plotted in terms of the tangential velocities that correspond to the mass distribution of each component. The CO rotation curve (tracing the total potential) is shown as the black dots with error bars (Section 3). The green stars show the measured stellar velocity curve for the fiducial value of Y_* listed in Table 3 (Section 4.1). The mass contributions from the atomic and molecular components (if available) are shown in red and orange (Section 4.2). The blue curves and shaded regions show the dark matter component, and the purple curves and shaded regions show the total modelled rotation curves of all the components (Equation 2), which should closely match the CO. The grey hatched region shows twice the CO beam HWHM, indicating the central regions which may be affected by beam smearing. The grey shaded region shows the radii over which β^* is calculated (Equation 6), and the best-fitting β^* values are listed in the upper left corners.

smaller physical radii in these galaxies than the definition used in many simulation-based analyses. This will be discussed further in Section 6 when we compare our results to simulations.

We also compute the central concentration (c_{200}) implied by our measurements, where $c_{200} \equiv \frac{R_{200}}{r_s} \equiv \frac{R_{\text{vir}}}{r_s}$ (e.g., Dutton & Macciò 2014; Newman et al. 2015). We report our values of c_{200} in Table 3,

where the uncertainties are substantial and propagated from the uncertainties on R_{vir} (Table 3) and r_s (Table B1). We compare with

Table 3. Fitted Stellar and Dark Matter Density Parameters

Name	Y_*	$R_{\max,*}$ (kpc)	$\log M_*$ ($< R_{\max,*}$) ($\log M_\odot$)	R_{vir} (kpc)	1–2% R_{vir} (kpc)	$\log M_{200}$ ($\log M_\odot$)	c_{200}	β^*	$\beta_{1-2\% R_{\text{vir}}}$
NGC 1035	0.21 ± 0.04	6.0	9.5	79^{+49}_{-21}	$0.8^{+0.5}_{-0.2} - 1.6^{+1.0}_{-0.4}$	$11.4^{+2.0}_{-0.3}$	27^{+22}_{-13}	$0.7^{+0.2}_{-0.2}$	$1.1^{+0.6}_{-0.4}$
NGC 4310	0.21 ± 0.04	6.2	9.3	64^{+30}_{-15}	$0.6^{+0.3}_{-0.1} - 1.3^{+0.6}_{-0.3}$	$11.2^{+1.4}_{-0.3}$	36^{+23}_{-13}	$0.4^{+0.4}_{-0.4}$	$0.8^{+0.7}_{-0.6}$
NGC 4451	0.21 ± 0.04	9.7	9.7	90^{+29}_{-14}	$0.9^{+0.3}_{-0.1} - 1.8^{+0.6}_{-0.3}$	$11.5^{+0.9}_{-0.2}$	40^{+20}_{-14}	$0.6^{+0.4}_{-0.5}$	$1.1^{+0.5}_{-0.6}$
NGC 4701	0.21 ± 0.04	6.5	9.4	65^{+40}_{-14}	$0.7^{+0.3}_{-0.2} - 1.3^{+0.8}_{-0.3}$	$11.1^{+2.3}_{-0.3}$	45^{+43}_{-24}	$0.4^{+0.8}_{-0.8}$	$0.9^{+1.0}_{-1.0}$
NGC 5692	0.83 ± 0.15	4.8	9.3	75^{+43}_{-12}	$0.8^{+0.4}_{-0.2} - 1.5^{+0.9}_{-0.2}$	$11.3^{+2.3}_{-0.2}$	46^{+47}_{-25}	$0.7^{+0.9}_{-1.0}$	$1.2^{+1.0}_{-1.1}$
NGC 6106	0.21 ± 0.04	8.9	9.7	68^{+15}_{-12}	$0.7^{+1.1}_{-0.1} - 1.4^{+2.3}_{-0.3}$	$11.2^{+15.5}_{-0.2}$	47^{+140}_{-20}	$0.7^{+0.3}_{-0.4}$	$1.1^{+1.1}_{-0.5}$

Y_* is the mass-to-light ratio assumed here reproduced from the stellar population synthesis model results presented by R19b. M_* is the total stellar mass within a radius $R_{\max,*}$ from the fitting described in Section 4.1; uncertainties are ± 0.1 dex. R_{vir} is the virial radius derived from the best-fitting total density profile, at which the density is $200\times$ the critical density. Uncertainties are propagated from the uncertainties on the total density profile. M_{200} is the mass contained within $R_{200} \equiv R_{\text{vir}}$. Uncertainties are propagated from R_{vir} . c_{200} is the concentration parameter, defined as R_{200}/r_s . Uncertainties are propagated from R_{vir} and r_s . β^* is the inner slope of the dark matter density profile, as defined in Equation 6. $\beta_{1-2\% R_{\text{vir}}}$ is the inner slope of the dark matter density profile measured from 1–2% of R_{vir} .

R19b where possible,⁷ and we agree within the (large) uncertainties on both calculations of c_{200} .

5 RESULTS

We are interested in measuring the inner slope of the dark matter density distribution for our sample of dwarf galaxies. We define ‘inner’ as from 0.3–0.8 kpc and denote the slope in this radial range as β^* (Equation 6). We use the CO rotation curves that we derive here (Figure 2; Section 3) as a robust tracer of the total potential. We use an MCMC method to construct model dark matter density profiles, assuming a gNFW form (Equation 3). By including the stellar component (Section 4.1), we minimize the difference between the CO rotation curve and our model circular velocity curve of the total potential (including the stars and dark matter; Section 4). We measure β^* from the fitted dark matter density profiles (Figure 4). Across this sample of galaxies, we find no trends between β^* and galaxy parameters such as inclination, distance, R_{\max} , R_{vir} , M_{dyn} , or M_* .

For these six galaxies, we find β^* values that are on average consistent with shallow cusp-like dark matter density profiles ($\langle \beta^* \rangle = 0.6$ with a standard deviation of ± 0.1 ; Table 3). We show the distribution of our β^* values in black in Figure 5 as a kernel density estimate (KDE). We make this KDE by summing the posterior distributions of β^* for each galaxy (Figure B1) and renormalising to unit area. The median of this distribution is $\tilde{\beta}^* = 0.5^{+0.4}_{-0.6}$, where the lower and upper uncertainties correspond to the 16th and 84th percentiles of the distribution (1- σ for a Gaussian distribution). By our KDE construction, this quoted uncertainty reflects both the measurement uncertainties and the galaxy-to-galaxy scatter (though counted in a different way than the standard deviation of the best-fitting values). The average and scatter derived from Table 3 ($\langle \beta^* \rangle = 0.6$ with standard deviation of ± 0.1) reflect only the galaxy-to-galaxy scatter in the best-fitting β^* values. The light grey distributions in Figure 5 show the posterior distributions of β^* for each galaxy (see also Figure B1).

We compare the distribution of our β^* measurements to those from R19b. A KDE of their values is shown in blue in Figure 5. For this

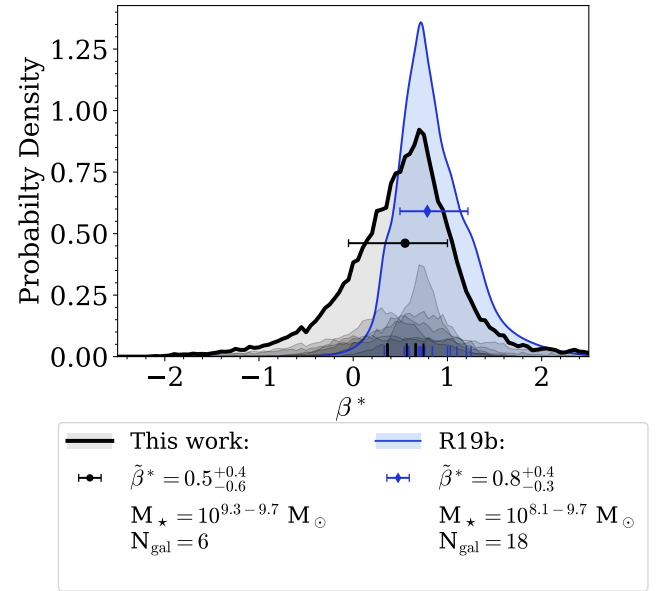


Figure 5. A KDE showing the distribution of β^* values we measure in this study (thick black curve). The light grey distributions show the posterior distributions of β^* for each galaxy, normalised to their fractional contribution to the total KDE (thick black curve). The black tick marks at the bottom show the individual β^* values; the error bars show the 16th and 84th percentiles. The blue KDE, tick marks, diamond, and error bars show the same quantities but for the galaxies studied by R19b with reliable mass decompositions. The legend also notes the number of galaxies in each KDE and the stellar mass range covered by those galaxies.

KDE, we represent each of their measurements as a Gaussian, where the width is set by their measurement uncertainties (see their Table 3, grades 1 and 2). The individual Gaussians are summed and normalised to unit area. Our distribution of the slopes is shifted towards somewhat shallower slopes than R19b, though there is substantial overlap between the distributions. In comparing these distributions, it is important to keep in mind that our sample only includes six galaxies, whereas R19b have 18 galaxies.

⁷ Though R19b do not report c_{200} directly, it is related to β and c_{-2} , which they report in their Table 4, where $c_{200} = c_{-2}(2-\beta)$. c_{-2} is the concentration measured at the radius at which $\rho \propto r^{-2}$ locally. See Newman et al. (2015) and R19b for more details.

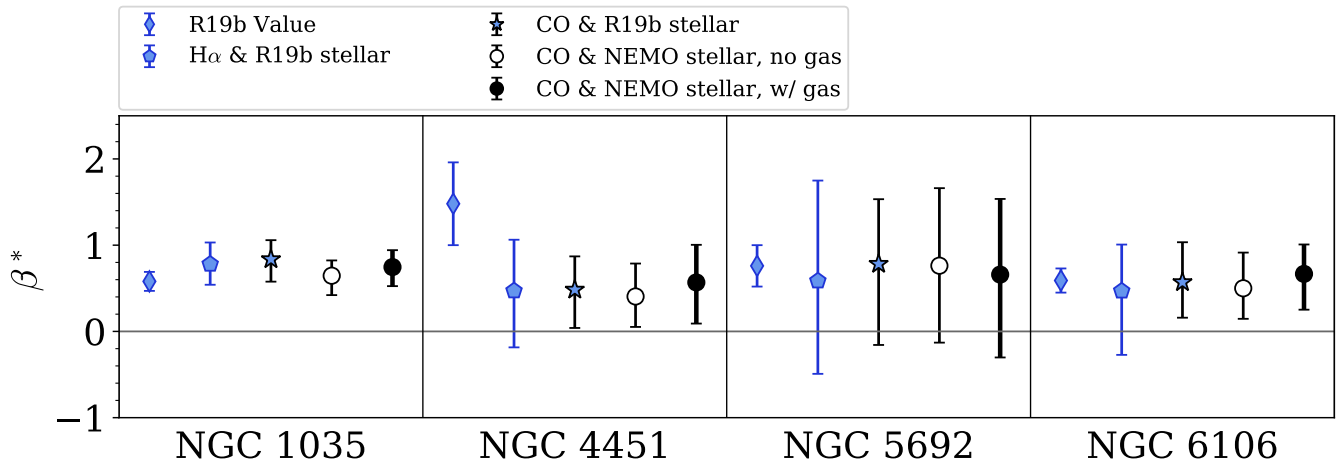


Figure 6. A comparison of the β^* values derived for different sets of assumptions as described in Section 5.1 for the galaxies that overlap with R19b. The blue diamonds show the values derived by R19b. The blue pentagons show the β^* we derive using H α rotation curves to trace the total potential (R19a), the stellar rotation curves from R19b, and including the atomic and molecular components as a check on the accuracy of our decomposition method. The blue filled stars show the results when using our CO rotation curves to trace the total potential, the stellar rotation curves from R19b, and including the atomic and molecular components. The circles show the values of β^* derived using our CO rotation curves to trace the total potential, the stellar rotation curves we derive using NEMO (Section 4.1), and either excluding (open) or including (filled) the atomic and molecular components. Within each galaxy bin, points are artificially offset along the horizontal axis for clarity. In general, we do not find significant differences in the values of β^* derived for each set of assumptions, given the uncertainties.

5.1 Checks on the method and assumptions

Below we describe several tests we performed to check the robustness of our modelling and results to various assumptions. We show the resulting values of β^* for these different tests in Figures 6 and B2. For the discussion in Section 6, we adopt the values of β^* we derive using our CO rotation curves and stellar velocity curves, including the atomic and molecular gas components where available, as reported in Table 3. In general, we do not find significant differences in the values of β^* derived for each set of assumptions given the uncertainties.

5.1.1 Decomposition method

As a check on our decomposition method, we measure β^* using the H α rotation curves from R19a as a tracer of the total potential and the stellar rotation curves from R19b to most closely reproduce their results. Any differences in these values compared to those presented by R19b are due to our fitting method, as the assumptions about the total and stellar potentials and the form of the dark matter density are the same.

As shown in Figure 6, the results of this test (blue pentagons) are in good agreement with the values reported by R19b (blue diamonds), meaning that our fitting routine does not introduce biases in the measurement of β^* . The most discrepant galaxy, in terms of the absolute differences in β^* , is NGC 4451, though the measurements are consistent within the uncertainties. In general, the uncertainties on our points are larger than those measured by R19b.

5.1.2 CO v. H α as tracers of the total potential

A difference between this analysis and that presented by R19b is that we use CO to trace the total potential while they use H α . As discussed in Section 3 (and by R19b), there is good agreement in general between the CO and H α rotation curves (Figure 2). For the H α , this indicates that it is indeed a dynamically cold tracer. The

low velocity dispersions of the CO (Table 2) confirm that it is also dynamically cold.

We compare the values of β^* we derive using the CO rotation curves (blue stars) with those we derive using the H α rotation curves from R19a (blue pentagons) in Figure 6. In both measurements, we use the stellar velocity curves derived by R19b to purely test the effect of the different tracers of the total potential. Given the uncertainties, the β^* measurements from CO and H α are in excellent agreement with one another.

5.1.3 Stellar velocity curve derivation

As described in Section 4.1, while we use the same photometric data to measure the stellar components as R19b, we derive the stellar light profiles and velocity curves using different methods and assumptions. As shown in Figure 3, the agreement between our derived stellar velocity curves is quite good in general.

In Figure 6, we compare the values of β^* derived using our stellar velocity curves (black filled circles) and those from R19b (blue stars), with all other variables the same. These values are in excellent agreement within the uncertainties. Therefore, our calculation of the stellar velocity components assuming a thin disk does not greatly affect the results.

5.1.4 Excluding the atomic and molecular components

We do not have information about the atomic and molecular mass components readily available for two of the galaxies in this sample. We test whether the measured β^* values are biased by not including the atomic and molecular gas in the mass decomposition. We repeat the decomposition to determine β^* with and without this gas data for the four galaxies that overlap between our sample and the R19b sample, using the CO data to trace the total potential and using our stellar velocity curves from NEMO. The β^* values with (filled circles) and without (open circles) the gas are compared directly in Figure 6.

For all galaxies, the derived β^* values are consistent well within the uncertainties. We therefore conclude that excluding the atomic and molecular gas data from the decomposition does not significantly affect the results.

5.1.5 Assumed functional form of the dark matter density profile

As we discuss in Appendix B, we re-run the decompositions and the aforementioned tests assuming a two parameter power-law dark matter density profile (instead of the gNFW profile given by Equation 3). The density profiles yield similar dark matter profiles and β^* values as the gNFW (Figure B2). This is likely because our CO observations probe small radii where the $(r/r_s)^\beta$ factor in the gNFW profile dominates, effectively reducing ρ_{DM} to a power-law. In some galaxies, the second factor in the gNFW profile does become important, as the power-law profiles continue to increase whereas the gNFW profiles soften and better represent the data. Therefore, we proceed with the results using the gNFW profiles.

6 DISCUSSION

6.1 Comparison to previous observational studies

We compare our measurements of the inner dark matter density slope to other observational studies of dwarf galaxies as a function of the stellar mass of the galaxy (Figure 7, top). These observational studies span a range of tracers and methodologies, as described briefly here. There is no overlap between our sample of galaxies and those from Simon et al. (2005), Oh et al. (2011, 2015), Adams et al. (2014), Li et al. (2019), or Leung et al. (2021). In Figure 7, we have tried to use similar colours for studies with similar methodologies, as described below.

Simon et al. (2005) use a combination of H α and CO data (where available) in five galaxies to measure β^* . The rotation curves were extracted using the same method as described in Section 3, and they fit their stellar rotation curves using a similar method to the one used here (Section 4.1). They measure their dark matter slopes from a power-law fit to the full dark matter velocity curves which extend out to 2–5 kpc from the centre. Assuming a fiducial $R_{\text{vir}} \sim 100$ kpc, these data probe $\sim 2 - 5$ per cent of R_{vir} . This corresponds to somewhat farther out in the dark matter halo than probed by our measurements which probe $\sim 0.3 - 1.6$ per cent of R_{vir} (see Section 4).

Adams et al. (2014) use integral field measurements, which trace the kinematics of the stars and ionized gas, in a sample of six dwarf galaxies. They extract their circular velocity curves using dynamical modeling of both the stars and ionized gas. As described by R19b, we use their gNFW fits to calculate β^* following Equation 6.

Oh et al. (2011, 2015) use HI data from the THINGS and LITTLE THINGS surveys to trace the galaxy potentials and *Spitzer* 3.6 μm data to remove the stellar contributions. They derive their rotation curves using a tilted ring model, which allows for radially varying geometric parameters to account for features such as warps, and apply an asymmetric drift correction to their data. Their method of deriving the stellar mass profiles is similar to ours, but using the 3.6 μm data. For their mass models, they use both a NFW profile (which produces a cusp) and a pseudo-isothermal model (which produces a core), finding that the pseudo-isothermal profiles are a better fit to their observations. They measure the inner slope of their dark matter density profiles by fitting a power-law at radii smaller than a ‘break’ radius, which is the radius where the slope changes most rapidly.

This break radius changes for each galaxy, but is $\lesssim 1$ kpc, so we are measuring β^* over a similar range of radii.

We note that Iorio et al. (2017) performed an independent re-analysis of the LITTLE THINGS data by fitting the kinematics of the HI data in three dimensions, rather than the two dimensional approach taken by Oh et al. (2011, 2015). Iorio et al. (2017) find that half of their rotation curves are consistent with those derived by Oh et al. (2015) within the uncertainties. For those galaxies where the rotation curves do differ, the slopes near the centres are not systematically steeper or shallower. In other words, if the mass modelling were repeated using the rotation curves from Iorio et al. (2017), we would not expect systematically steeper (or shallower) dark matter density profiles compared to Oh et al. (2015).

As discussed previously, R19b use H α measurements to trace the total potential of the galaxies and *Spitzer* 4.5 μm data to trace the stellar components. They obtain their stellar profiles using a multi-Gaussian expansion method, as opposed to our method of extracting the stellar light in concentric annuli. We base our decomposition method on theirs and adopt their definition of β^* . Figure 6 shows the comparison of our β^* measurements to theirs for the four common galaxies.

Li et al. (2019) derive dark matter mass models for the 175 galaxies in the *Spitzer* Photometry and Accurate Rotation Curves (SPARC) data base (Lelli et al. 2016). The SPARC galaxies span a broad range of morphologies, luminosities, and surface brightnesses. Their rotation curves tracing the total potential of the galaxies come from either HI or H α data. The stellar components are traced by *Spitzer* 3.6 μm data. The stellar mass estimates come from Lelli et al. (2016), assuming $Y_\star = 0.5$, though Lelli et al. (2016) note that there are disagreements between this value and other studies. For the mass models, we use the Di Cintio et al. (2014) fits (a version of the gNFW profile) with flat priors from Li et al. (2019) to reconstruct their dark matter density profiles (see their Table A2). From these, we measure β^* according to Equation 6.

Leung et al. (2021) use HI data and stellar dynamical modelling to constrain the dark matter distribution in the dwarf irregular galaxy WLM. They use a gNFW profile, but also allow for flattening of the dark matter distribution, finding a prolate geometry is favoured. Their reported best-fitting value of the dark matter density slope is β in the gNFW profile (not β^* ; Equation 3). To best compare with our measurements, we use their value of the dark matter slope for a spherical dark matter distribution including the gas and stars ($0.27^{+0.25}_{-0.17}$) which agrees within the uncertainty with their best-fitting slope allowing the dark matter geometry to vary.

From the observations, there is a general trend of lower mass galaxies exhibiting core-like inner dark matter density profiles with slopes $\beta^* \sim 0$ (Figure 7, top), though this trend is driven by the results of Oh et al. (2011, 2015) and supported by Leung et al. (2021) and Li et al. (2019). Higher mass galaxies—like those in this study—tend to have cuspy dark matter density slopes ($\beta^* \gtrsim 0.5$), but the scatter is large. In general, our measurements of β^* agree well with other observations at similar stellar masses (Figure 7, top).

Observations of dwarf galaxies at similar stellar masses also show a wide range of dark matter density slopes (Figure 7, top). While this scatter may reflect real galaxy-to-galaxy variations, uncertainties in the rotation curves and differences in how β^* is measured likely contribute to the scatter, perhaps substantially (see discussions in, for example, R19b and Santos-Santos et al. 2020). We find no clear trends between β^* and galaxy properties such as M_\star , M_{dyn} , or R_{vir} . Similarly, R19b find no trends between β^* and the galaxy effective radius and stellar surface density in the inner kpc of the galaxy. Some recent simulations also confirm or reproduce this observed diversity

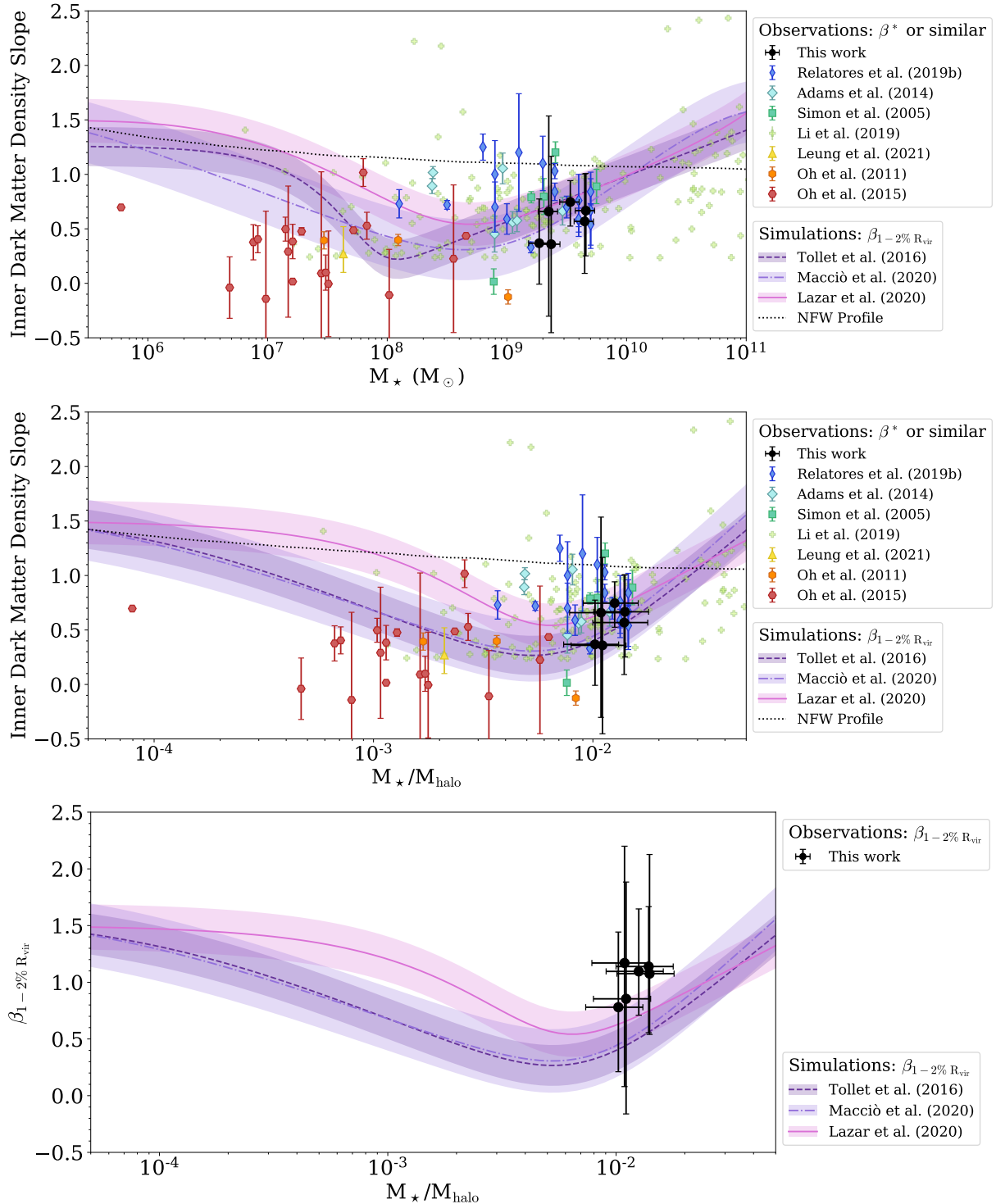


Figure 7. The inner slope of the dark matter density profile as a function of stellar mass (top) and the ratio of stellar mass to halo mass (middle). There are several definitions and methods of measuring the inner slope of the dark matter density profile shown in this figure. The β^* values derived here are shown in the black circles. The horizontal error bars on our points reflect the uncertainty in our stellar mass measurements (top) or the scatter in the assumed stellar mass-halo mass relation (bottom). We compare with other observational studies (colored symbols; [Simon et al. 2005](#); [Oh et al. 2011, 2015](#); [Adams et al. 2014](#); [Relatores et al. 2019b](#); [Li et al. 2019](#); [Leung et al. 2021](#)) and predictions from the NIHAO ([Tollet et al. 2016](#); [Macciò et al. 2020](#)) and FIRE ([Lazar et al. 2020](#)) simulations (shaded curves). The black dotted line shows the expectation from an NFW profile. Cores have $\beta^* \sim 0$ and cusps have $\beta^* \gtrsim 0.5$. Our measurements are in good agreement with previous measurements at similar M_* and M_*/M_{halo} , given the scatter and uncertainties. Galaxies in this range of M_* and M_*/M_{halo} tend to have cuspy dark matter density profiles. The bottom panel shows $\beta_{1-2\% R_{\text{vir}}}$ for our measurements compared to the NIHAO ([Tollet et al. 2016](#); [Macciò et al. 2020](#)) and FIRE ([Lazar et al. 2020](#)) simulations. When the inner slopes of the dark matter density profiles are measured in the same way, our measurements tend to be steeper than predicted by these simulations.

in the dark matter density profiles at fixed stellar mass (e.g., Oman et al. 2015, 2019; Kamada et al. 2017; Santos-Santos et al. 2018, 2020; Orkney et al. 2021).

6.2 Comparison to simulations

We also compare our measurements to those from simulations (Figure 7) as a function of both the stellar mass and the ratio of the stellar mass to the halo mass (M_\star/M_{halo}). The curves show the results from the FIRE (Lazar et al. 2020) and NIHAO (Tollet et al. 2016; Macciò et al. 2020) simulations. The simulations measure β^* from 1 – 2 per cent of R_{vir} , as opposed to the fixed radial range of 0.3 – 0.8 kpc we use (Equation 6).

We convert the curve presented by Lazar et al. (2020) in terms of M_\star/M_{halo} to M_\star using their stellar mass-halo mass relation (see their Figure 1)⁸. We use this same relation to convert the observations from M_\star to M_\star/M_{halo} ⁹. The horizontal errorbars on our points in the middle and bottom panels of Figure 7 include the scatter in the stellar mass-halo mass relation in addition to the uncertainties on the stellar mass measurements.

The above simulations predict a stellar mass range ($M_\star \sim 10^{7.5-9.5} M_\odot$) where feedback is efficient in softening the dark matter density profile in the centres of galaxies. In reality, this trend depends on M_\star/M_{halo} and evolves with time (e.g., Di Cintio et al. 2014; Tollet et al. 2016). For example, Tollet et al. (2016) find that all galaxies begin with cuspy profiles. For low mass galaxies, Tollet et al. (2016) find that the central regions evolve passively once star formation has finished, and so they retain their cuspy profiles until $z = 0$. Other groups, however, find that very low mass systems can develop core-like profiles due to late-time minor mergers (Orkney et al. 2021) or starburst phases (Read et al. 2016). For galaxies of intermediate M_\star/M_{halo} , the amount of gas is rapidly changing due to inflows, accretion of satellites, mergers, and star formation-driven outflows. As a result, the potential undergoes rapid changes and the centre of mass of the gas changes with respect to the dark matter, both of which help develop and maintain the core-like density profile (Tollet et al. 2016). For the most massive galaxies, cores may form due to accretion and stellar feedback, resulting in rapid changes in M_\star/M_{halo} in the central regions as for the intermediate-mass systems. However, Tollet et al. (2016) find that the net result for these higher mass galaxies is that gas flows inward towards the centre, triggering more star formation and hence increasing the stellar mass relative to the halo mass in the centre. As the potential well deepens due to the gas inflows, feedback-driven outflows become less important in terms of expelling mass. As a result of the deepened central potential, dark matter becomes concentrated at the centre and hence the cuspy

⁸ We note that the stellar mass-halo mass relation in Lazar et al. (2020) quantifies the typical stellar mass at fixed halo mass. However, for our conversions, we require the halo mass at fixed stellar mass. These conversions are not necessarily the same (e.g., Behroozi et al. 2010). However, for the range of masses considered here, this is likely a small effect. This is substantiated by the fact that the M_{halo} values implied by this conversion agree well with our estimates of M_{200} .

⁹ As part of their fitting, Li et al. (2019) report M_\star/M_{halo} values for the SPARC galaxies. However, the definitions of the slope parameters in the Di Cintio et al. (2014) dark matter profiles depend explicitly on M_\star/M_{halo} , and there is a strong correlation between β^* and M_\star/M_{halo} induced by this relation. Therefore, for the points from Li et al. (2019) shown in the bottom panel of Figure 7, we recompute M_\star/M_{halo} using the independently measured stellar masses from Lelli et al. (2016) and the same stellar mass-halo mass relation as for the other observations.

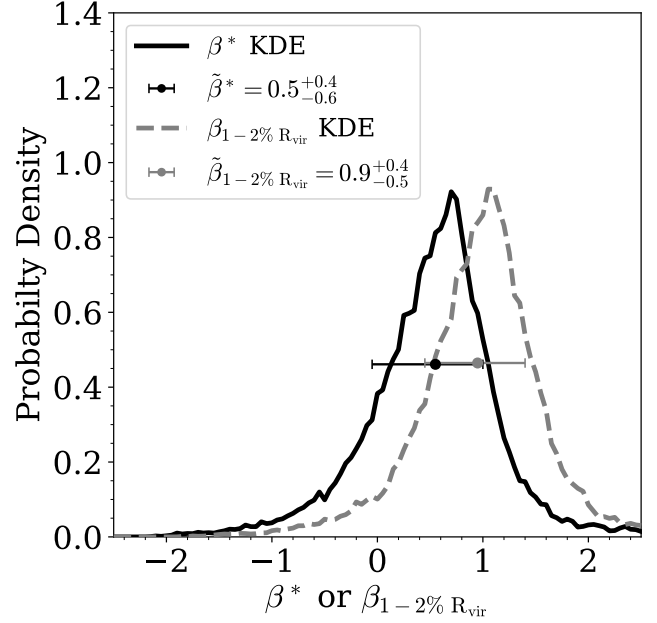


Figure 8. KDEs comparing the inner slope of the dark matter density profile as parametrized by β^* (black solid) or $\beta_{1-2\% R_{\text{vir}}}$ (grey dashed). The black and grey dots show the median of each distribution; the error bars show the 16th and 84th percentiles. The β^* KDE is the same as in Figure 5. The dark matter slopes parametrized by $\beta_{1-2\% R_{\text{vir}}}$ are steeper than β^* .

profile is restored. There is some evidence from simulations that Milky Way mass galaxies ($M_\star \approx 10^{10-11} M_\odot$, $M_{\text{halo}} \sim 10^{12} M_\odot$) can retain small (0.5 – 2 kpc) cores, which are maintained by stellar feedback (Chan et al. 2015; Lazar et al. 2020). Outflows from active galactic nuclei can also soften the cuspy profile in the most massive galaxies ($M_{\text{halo}} > 10^{12} M_\odot$), though the slopes are still within the cusp-like regime (Macciò et al. 2020).

The galaxies in this study have $M_\star = 10^{8.9-9.7} M_\odot$. Assuming a stellar mass-halo mass relation like Lazar et al. (2020) implies $M_{\text{halo}} \approx 10^{11.0-11.5} M_\odot$. This agrees with our estimates of M_{200} (as an approximation of M_{halo} to within ~ 90 per cent¹⁰) listed in Table 3 within the uncertainties. Therefore, for these relatively massive dwarfs at $z = 0$, we would expect to find more cuspy dark matter profiles, which we quantitatively confirm with these measurements.

As discussed in Section 4.3, our definition of β^* probes smaller radii than the simulations. The simulations measure the slope of the dark matter density profile from radii between 1 – 2 per cent of R_{vir} , which we report in Table 3. However, our adopted definition of β^* (Equation 6) covers a fixed radial range from 0.3 – 0.8 kpc, which corresponds to ~ 0.3 – 1.6 per cent of R_{vir} for these galaxies. In an effort to best compare with simulations, we also compute $\beta_{1-2\% R_{\text{vir}}}$, given our estimates of R_{vir} and its uncertainties in Table 3. Like β^* , $\beta_{1-2\% R_{\text{vir}}}$ is calculated at every step in the MCMC chain during the decomposition, and hence β^* and $\beta_{1-2\% R_{\text{vir}}}$ are calculated for the same dark matter density profile at each step and any differences between them reflects only the differences in the definitions of β^* and $\beta_{1-2\% R_{\text{vir}}}$. The uncertainty on $\beta_{1-2\% R_{\text{vir}}}$ also incorporates the

¹⁰ Lazar et al. (2020) adopt the virial definition of the halo mass from Bryan & Norman (1998), in which the virial overdensity is ~ 100 times the critical density. Under this definition, $M_{\text{halo}}/M_{200} \sim 1.1$. This difference is less than the scatter in Figure 7 and is, therefore, only a minor concern for this analysis.

uncertainty on R_{vir} . We report our best-fitting $\beta_{1-2\% R_{\text{vir}}}$ values in Table 3. Figure 8 compares the KDEs of β^* and $\beta_{1-2\% R_{\text{vir}}}$, which are the sums of the posterior distributions over all of the galaxies normalised to unit area. The distribution of $\beta_{1-2\% R_{\text{vir}}}$ is shifted towards steeper slopes than the distribution of β^* . We compare our $\beta_{1-2\% R_{\text{vir}}}$ measurements to the simulations in Figure 7 (bottom).

When the measured dark matter density slope is parametrized by β^* , most of our measured points agree with the predictions from the FIRE and NIHAO simulations (Figure 7, top and middle). Observations at similar M_\star and M_\star/M_{halo} show a similar distribution of β^* , though the scatter is large (see also Figure 5). If we instead use $\beta_{1-2\% R_{\text{vir}}}$ as our parametrization of the inner dark matter density slope—which is the value reported by the simulations—we find that most of our galaxies have steeper dark matter density profiles than predicted by these simulations (Figure 7, bottom). Therefore, in this most equal comparison, our observations tend to have cuspid dark matter profiles than predicted by the FIRE and NIHAO simulations.

As described above, one way for a galaxy to restore a cuspy profile is through gas inflows which trigger a burst of star formation. This both deepens the potential well, causing dark matter to concentrate in the centre of the galaxy, and increases the stellar mass of the centre relative to the halo mass. One possible explanation for the more cuspy profiles observed in these (and other) galaxies is that these galaxies had stronger gas inflows towards the centre than predicted by the simulations, resulting in more centrally concentrated dark matter at the centres. An alternate possibility is that the simulations overpredict the strength or frequency of accretion, merger, and/or outflow events for galaxies in this stellar mass range. As described by Tollet et al. (2016), these feedback events stir up the potential, allowing the dark matter distribution to be shallower and maintaining a core-like central profile. If there were less frequent or intense accretion or outflows, the dip in the curves from simulations shown in Figure 7 would be both shallower and narrower. It is also possible that both effects are at work, or that there are other factors responsible for this population of galaxies with cuspy profiles given their M_\star and M_\star/M_{halo} .

7 SUMMARY

We have investigated the inner slope of the dark matter density distribution (β^*) using observations of six nearby spiral dwarf galaxies. We summarize our results below.

(i) Using new CO observations from ALMA, we measure the CO rotation curves of these galaxies, which provide a dynamically cold tracer of the total potential (Section 3, Figure 2). We find excellent agreement between the CO and H α rotation curves in 3/4 galaxies where both are available.

(ii) We decompose the dark matter velocity curve and density profile using an MCMC method, knowing the total potential and the contribution from the stars (Section 4, Figure 4). From these, we measure β^* , finding $\langle \beta^* \rangle = 0.6$ with a standard deviation of ± 0.1 among the best-fitting β^* values for galaxies in this sample (Table 3). Considering the full posterior distributions of β^* , the median β^* for this sample is $\tilde{\beta}^* = 0.5_{-0.6}^{+0.4}$, where the lower and upper uncertainties correspond to the 16th and 84th percentiles of the distribution (Figure 5).

(iii) We find that the relatively massive dwarf galaxies ($M_\star = 10^{9.3-9.7} M_\odot$) in this study show cuspid dark matter distributions than lower mass dwarf galaxies, in agreement with other observations at similar M_\star and M_\star/M_{halo} (Figures 5 and 7).

(iv) To accurately compare our measurements with results from the FIRE and NIHAO simulations, we compute $\beta_{1-2\% R_{\text{vir}}}$ for our galaxies. The inner dark matter density slopes parametrized by $\beta_{1-2\% R_{\text{vir}}}$ are steeper than β^* (Figure 8). We find that our galaxies have steeper slopes on average than predicted by the FIRE and NIHAO simulations (Figure 7, bottom). This may signal that these galaxies have undergone a stronger gas inflow than implemented in the simulations, that the simulations overpredict the frequency of accretion/merger/outflow events, or that a combination of these or other effects are at work.

Analyses such as these are often limited by the sensitivity needed to probe out to large radii in faint, often gas-poor dwarf galaxies. Future facilities, especially the Next Generation Very Large Array, will transform our ability to measure gas kinematics in dwarf galaxies. Owing to its increased sensitivity and angular resolution and the ability to observe both CO and HI, we can trace the rotation curves out to larger radii more robustly. The increased spatial resolution will allow for more accurate measurements in the centres, precisely in the range of radii where β^* is measured. Finally, the combination of the increased resolution and sensitivity will allow us to probe lower mass and more distant systems to better understand how the dark matter distributions change over time and as a function of environment.

ACKNOWLEDGEMENTS

The authors sincerely thank the anonymous referee for their thoughtful and constructive feedback that greatly improved this paper. We also gratefully acknowledge the work of Leo Blitz, who wrote and led the ALMA proposal to obtain the data upon which this work is based. L.H.C. and B.D.D. thank the Department of Astronomy at the University of Maryland for hosting them during the completion of this work. R.C.L. acknowledges partial support for this work provided by the National Science Foundation (NSF) through Student Observing Support Program (SOSP) award 7-011 from the NRAO and by an NSF Astronomy and Astrophysics Postdoctoral Fellowship under award AST-2102625. A.D.B. acknowledges partial support from NSF-AST2108140. B.D.D. acknowledges funding and support from the Graduate Resources Advancing Diversity with Maryland Astronomy and Physics (GRAD-MAP) program (www.umdgradmap.org), which is funded by the University of Maryland College of Computer, Mathematical, and Natural Sciences and the Departments of Astronomy and Physics and the NSF PIRE (Grant No. 1545949) and AAG (Grant No. AST-1615960) programs. V.V. acknowledges support from the scholarship ANID-FULBRIGHT BIO 2016 - 56160020 and funding from NRAO through SOSP award SOSPA7-014.

This paper makes use of the following ALMA data: ADS/JAO.ALMA#2015.1.00820.S. ALMA is a partnership of ESO (representing its member states), NSF (USA) and NINS (Japan), together with NRC (Canada), NSC and ASIAA (Taiwan), and KASI (Republic of Korea), in cooperation with the Republic of Chile. The Joint ALMA Observatory is operated by ESO, AUI/NRAO and NAOJ. The National Radio Astronomy Observatory is a facility of the National Science Foundation operated under cooperative agreement by Associated Universities, Inc. This work is based in part on observations made with the *Spitzer* Space Telescope, which was operated by the Jet Propulsion Laboratory, California Institute of Technology under a contract with NASA. The Pan-STARRS1 Surveys (PS1) and the PS1 public science archive have been made possible through contributions by the Institute for Astronomy, the University of Hawaii, the Pan-STARRS Project Office, the Max-Planck Society and its participating institutes, the Max Planck In-

stitute for Astronomy, Heidelberg and the Max Planck Institute for Extraterrestrial Physics, Garching, The Johns Hopkins University, Durham University, the University of Edinburgh, the Queen's University Belfast, the Harvard-Smithsonian Center for Astrophysics, the Las Cumbres Observatory Global Telescope Network Incorporated, the National Central University of Taiwan, the Space Telescope Science Institute, the National Aeronautics and Space Administration under Grant No. NNX08AR22G issued through the Planetary Science Division of the NASA Science Mission Directorate, the National Science Foundation Grant No. AST-1238877, the University of Maryland, Eotvos Lorand University (ELTE), the Los Alamos National Laboratory, and the Gordon and Betty Moore Foundation. This study makes use of numerical values from the HyperLEDA database (<http://leda.univ-lyon1.fr>). This research has made use of NASA's Astrophysics Data System Bibliographic Services. This research made use of Astropy (Astropy Collaboration et al. 2018), CASA (McMullin et al. 2007), corner (Foreman-Mackey 2016), EMCEE (Foreman-Mackey et al. 2013), Matplotlib (Caswell et al. 2020), MIRIAD (Sault et al. 1995), NEMO (Teuben 1995), NumPy (Harris et al. 2020), pandas (Reback et al. 2020), photutils (Bradley et al. 2018), SciPy (Virtanen et al. 2020), and seaborn (Waskom et al. 2014).

DATA AVAILABILITY

The ALMA data used for this study are part of program ADS/JAO.ALMA#2015.1.00820.S and are publicly available on the ALMA Science Archive (<https://almascience.nrao.edu/asax/>). The data products used in this analysis can be downloaded at <https://github.com/rclevy/RotationCurveFiltedRings>. The *Spitzer* images are publicly available on the NASA/IPAC Infrared Science Archive (<https://irsa.ipac.caltech.edu/>). The PS1 data are publicly available on the PS1 Image Cutout Server (<https://ps1images.stsci.edu/cgi-bin/ps1cutouts>).

REFERENCES

- Adams J. J., et al., 2014, *ApJ*, **789**, 63
 Astropy Collaboration et al., 2018, *AJ*, **156**, 123
 Begeman K. G., 1987, PhD thesis, Kapteyn Institute
 Begeman K. G., 1989, *A&A*, **223**, 47
 Behroozi P. S., Conroy C., Wechsler R. H., 2010, *ApJ*, **717**, 379
 Bolatto A. D., Simon J. D., Leroy A., Blitz L., 2002, *ApJ*, **565**, 238
 Bosma A., 1978, PhD thesis, Groningen Univ.
 Bradley L., et al., 2018, astropy/photutils: v0.5, doi:10.5281/zenodo.1340699, <http://doi.org/10.5281/zenodo.1340699>
 Bryan G. L., Norman M. L., 1998, *ApJ*, **495**, 80
 Bullock J. S., Boylan-Kolchin M., 2017, *ARA&A*, **55**, 343
 Caswell T. A., et al., 2020, matplotlib/matplotlib: REL: v3.3.2, doi:10.5281/zenodo.4030140, <https://doi.org/10.5281/zenodo.4030140>
 Chambers K. C., et al., 2016, arXiv e-prints, p. arXiv:1612.05560
 Chan T. K., Kereš D., Oñorbe J., Hopkins P. F., Muratov A. L., Faucher-Giguère C. A., Quataert E., 2015, *MNRAS*, **454**, 2981
 Correa C. A., 2021, *MNRAS*, **503**, 920
 Cyr-Racine F.-Y., Sigurdson K., Zavala J., Bringmann T., Vogelsberger M., Pfrommer C., 2016, *Phys. Rev. D*, **93**, 123527
 de Blok W. J. G., Bosma A., 2002, *A&A*, **385**, 816
 de Blok W. J. G., McGaugh S. S., Rubin V. C., 2001a, *AJ*, **122**, 2396
 de Blok W. J. G., McGaugh S. S., Bosma A., Rubin V. C., 2001b, *ApJ*, **552**, L23
 Di Cintio A., Brook C. B., Macciò A. V., Stinson G. S., Knebe A., Dutton A. A., Wadsley J., 2014, *MNRAS*, **437**, 415
 Di Valentino E., et al., 2021, *Classical and Quantum Gravity*, **38**, 153001
 Dutton A. A., Macciò A. V., 2014, *MNRAS*, **441**, 3359
 Elbert O. D., Bullock J. S., Garrison-Kimmel S., Rocha M., Oñorbe J., Peter A. H. G., 2015, *MNRAS*, **453**, 29
 Fitts A., et al., 2017, *MNRAS*, **471**, 3547
 Flores R. A., Primack J. R., 1994, *ApJ*, **427**, L1
 Foreman-Mackey D., 2016, *The Journal of Open Source Software*, **1**, 24
 Foreman-Mackey D., Hogg D. W., Lang D., Goodman J., 2013, *PASP*, **125**, 306
 Fry A. B., et al., 2015, *MNRAS*, **452**, 1468
 Garcia A. M., 1993, *A&AS*, **100**, 47
 Genina A., et al., 2018, *MNRAS*, **474**, 1398
 Governato F., et al., 2012, *MNRAS*, **422**, 1231
 Harris C. R., et al., 2020, *Nature*, **585**, 357–362
 Hayashi E., Navarro J. F., 2006, *MNRAS*, **373**, 1117
 Hopkins P. F., et al., 2018, *MNRAS*, **480**, 800
 Iorio G., Fraternali F., Nipoti C., Di Teodoro E., Read J. I., Battaglia G., 2017, *MNRAS*, **466**, 4159
 Jahn E. D., et al., 2021, *MNRAS*, p. arXiv:2110.00142
 Kamada A., Kaplinghat M., Pace A. B., Yu H.-B., 2017, *Phys. Rev. Lett.*, **119**, 111102
 Kaplinghat M., Ren T., Yu H.-B., 2020, *J. Cosmology Astropart. Phys.*, **2020**, 027
 Kregel M., van der Kruit P. C., de Grijs R., 2002, *MNRAS*, **334**, 646
 Lazar A., et al., 2020, *MNRAS*, **497**, 2393
 Lelli F., 2022, *Nature Astronomy*, **6**, 35
 Lelli F., McGaugh S. S., Schombert J. M., 2016, *AJ*, **152**, 157
 Leung G. Y. C., et al., 2018, *MNRAS*, **477**, 254
 Leung G. Y. C., Leaman R., Battaglia G., van de Ven G., Brooks A. M., Peñarrubia J., Venn K. A., 2021, *MNRAS*, **500**, 410
 Levy R. C., et al., 2018, *ApJ*, **860**, 92
 Li P., Lelli F., McGaugh S. S., Starkman N., Schombert J. M., 2019, *MNRAS*, **482**, 5106
 Macciò A. V., Crespi S., Blank M., Kang X., 2020, *MNRAS*, **495**, L46
 Makarov D., Prugniel P., Terekhova N., Courtois H., Vauglin I., 2014, *A&A*, **570**, A13
 Maller A. H., Flores R. A., Primack J. R., 1997, *ApJ*, **486**, 681
 Marasco A., Oman K. A., Navarro J. F., Frenk C. S., Oosterloo T., 2018, *MNRAS*, **476**, 2168
 McMullin J. P., Waters B., Schiebel D., Young W., Golap K., 2007, in Shaw R. A., Hill F., Bell D. J., eds, *Astronomical Society of the Pacific Conference Series Vol. 376, Astronomical Data Analysis Software and Systems XVI*, p. 127
 Moore B., 1994, *Nature*, **370**, 629
 Moore B., Ghigna S., Governato F., Lake G., Quinn T., Stadel J., Tozzi P., 1999, *ApJ*, **524**, L19
 Muñoz-Mateos J. C., et al., 2013, *ApJ*, **771**, 59
 Navarro J. F., Eke V. R., Frenk C. S., 1996a, *MNRAS*, **283**, L72
 Navarro J. F., Frenk C. S., White S. D. M., 1996b, *ApJ*, **462**, 563
 Newman A. B., Belli S., Ellis R. S., 2015, *ApJ*, **813**, L7
 Oguri M., Takada M., Umetsu K., Broadhurst T., 2005, *ApJ*, **632**, 841
 Oh S.-H., de Blok W. J. G., Walter F., Brinks E., Kennicutt Robert C. J., 2008a, *AJ*, **136**, 2761
 Oh S.-H., Kim W.-T., Lee H. M., Kim J., 2008b, *ApJ*, **683**, 94
 Oh S.-H., Brook C., Governato F., Brinks E., Mayer L., de Blok W. J. G., Brooks A., Walter F., 2011, *AJ*, **142**, 24
 Oh S.-H., et al., 2015, *AJ*, **149**, 180
 Oman K. A., et al., 2015, *MNRAS*, **452**, 3650
 Oman K. A., Marasco A., Navarro J. F., Frenk C. S., Schaye J., Benítez-Llambay A., 2019, *MNRAS*, **482**, 821
 Orkney M. D. A., et al., 2021, *MNRAS*, **504**, 3509
 Peter A. H. G., Rocha M., Bullock J. S., Kaplinghat M., 2013, *MNRAS*, **430**, 105
 Pontzen A., Governato F., 2014, *Nature*, **506**, 171
 Querejeta M., et al., 2015, *ApJS*, **219**, 5
 Reach W. T., et al., 2005, *PASP*, **117**, 978

- Read J. I., Iorio G., Agertz O., Fraternali F., 2016, *MNRAS*, **462**, 3628
- Read J. I., Walker M. G., Steger P., 2018, *MNRAS*, **481**, 860
- Reback J., et al., 2020, pandas-dev/pandas: Pandas 1.1.3, doi:10.5281/zenodo.4067057, <https://doi.org/10.5281/zenodo.4067057>
- Relatores N. C., et al., 2019a, *ApJ*, **873**, 5
- Relatores N. C., et al., 2019b, *ApJ*, **887**, 94
- Riess A. G., Casertano S., Yuan W., Bowers J. B., Macri L., Zinn J. C., Scolnic D., 2021, *ApJ*, **908**, L6
- Sagunski L., Gad-Nasr S., Colquhoun B., Robertson A., Tulin S., 2021, *J. Cosmology Astropart. Phys.*, **2021**, 024
- Santos-Santos I. M., Di Cintio A., Brook C. B., Macciò A., Dutton A., Domínguez-Tenreiro R., 2018, *MNRAS*, **473**, 4392
- Santos-Santos I. M. E., et al., 2020, *MNRAS*, **495**, 58
- Sault R. J., Teuben P. J., Wright M. C. H., 1995, in Shaw R. A., Payne H. E., Hayes J. J. E., eds, *Astronomical Society of the Pacific Conference Series Vol. 77, Astronomical Data Analysis Software and Systems IV*. p. 433 ([arXiv:astro-ph/0612759](https://arxiv.org/abs/astro-ph/0612759))
- Sheth K., et al., 2010, *PASP*, **122**, 1397
- Simon J. D., Bolatto A. D., Leroy A., Blitz L., 2003, *ApJ*, **596**, 957
- Simon J. D., Bolatto A. D., Leroy A., Blitz L., Gates E. L., 2005, *ApJ*, **621**, 757
- Spergel D. N., Steinhardt P. J., 2000, *Phys. Rev. Lett.*, **84**, 3760
- Teuben P., 1995, in Shaw R. A., Payne H. E., Hayes J. J. E., eds, *Astronomical Society of the Pacific Conference Series Vol. 77, Astronomical Data Analysis Software and Systems IV*. p. 398
- Teuben P. J., 2002, in Athanassoula E., Bosma A., Mujica R., eds, *Astronomical Society of the Pacific Conference Series Vol. 275, Disks of Galaxies: Kinematics, Dynamics and Perturbations*. pp 217–228 ([arXiv:astro-ph/0204471](https://arxiv.org/abs/astro-ph/0204471))
- Tollet E., et al., 2016, *MNRAS*, **456**, 3542
- Tonry J. L., et al., 2012, *ApJ*, **750**, 99
- Truong P. N., Newman A. B., Simon J. D., Blitz L., Ellis R., Bolatto A., 2017, *ApJ*, **843**, 37
- Tully R. B., et al., 2013, *AJ*, **146**, 86
- Valli M., Yu H.-B., 2018, *Nature Astronomy*, **2**, 907
- van der Kruit P. C., Allen R. J., 1978, *ARA&A*, **16**, 103
- Virtanen P., et al., 2020, *Nature Methods*, **17**, 261
- Vogelsberger M., Zavala J., Loeb A., 2012, *MNRAS*, **423**, 3740
- Vogelsberger M., Zavala J., Cyr-Racine F.-Y., Pfrommer C., Bringmann T., Sigurdson K., 2016, *MNRAS*, **460**, 1399
- Walter F., Dahlem M., Lisenfeld U., 2004, *ApJ*, **606**, 258
- Warner P. J., Wright M. C. H., Baldwin J. E., 1973, *MNRAS*, **163**, 163
- Waskom M., et al., 2014, Seaborn: V0.5.0 (November 2014), doi:10.5281/zenodo.12710
- Willmer C. N. A., 2018, *ApJS*, **236**, 47
- Yoshida N., Springel V., White S. D. M., Tormen G., 2000, *ApJ*, **544**, L87
- Zhao H., 1996, *MNRAS*, **278**, 488

APPENDIX A: DETAILS OF THE ROTATION CURVE FITTING

As a check on the rotation curve fitting, we compute the residual velocity field for each galaxy. We construct a model velocity field from the best-fitting harmonic decomposition (Equation 1). The residual velocity fields are the difference between observed CO velocity fields and the models ($V_{\text{CO}} - V_{\text{model}}$) and are shown in Figure A1. In general, the residual velocities are small with no distinguishable patterns that may indicate improper geometric parameters (e.g., van der Kruit & Allen 1978). In NGC 4310, there are small residuals near the centre. Because these residuals are small and near the centre (which is excluded from the analysis), they have a negligible effect. In NGC 4451, the residual velocities are positive along the spiral arms. The magnitudes of these residual velocities are small, so they likely have only a minor effect on the robustness of the derived rotation

curve. In principle, we could use a higher order harmonic decomposition that could better represent the spiral arms. However, given the relatively few angular bins in our CO rotation curves, a higher order fit would likely be poorly constrained.

APPENDIX B: FITTING THE DARK MATTER PROFILES

The MCMC method used to decompose the dark matter density profile is described in Section 4, and the final fitted parameters and uncertainties are reported in Table B1. We show the posterior distributions of the fitted parameters for each galaxy in Figure B1. While some of the posterior distributions are wide, the value of β^* is relatively insensitive to the precise individual values of ρ_0 , r_s , and β . Rather, it is the combination of these parameters yielding the dark matter density distribution that determines the value of β^* .

In addition to the gNFW profile in Equation 3, we also tried a single power-law of the form

$$\rho_{\text{DM}}(r) = Ar^{-\beta} \quad (\text{B1})$$

since our CO observations tend to probe small radii close to the centre and the three-parameter fits shown in Figure B1 appear under-constrained. The posteriors of the power-law fits are good and, in general, better constrained than the three-parameter gNFW fits. The resulting power-law model rotation curves, however, tend to continue rising whereas the CO rotation curves tracing the total potential flatten. This suggests that while the CO observations tend to probe close to the galaxy centres, they do reach the radial range where a second power-law slope may be important. This is most evident for NGC 6106, which has the largest R_{max} in the sample. The power-law fit continues to rise, producing a steeper dark matter slope in the centre, resulting in the slightly larger values of β^* compared to the gNFW, all else being equal. We directly compare the derived values of β^* in Figure B2. For the same assumptions about the gas content and stellar profiles used (see Section 5.1), the β^* values from the power-law and gNFW dark matter density profiles are consistent within the uncertainties.

These tests show that while the precise values for the gNFW dark matter density profile parameters may be under-constrained, their combination and hence the derivation of β^* is fairly robust. R19b also found that β^* itself is better constrained than the individual gNFW parameters. We therefore adopt the β^* values from the more physically motivated gNFW profile in the discussion.

This paper has been typeset from a $\text{\TeX}/\text{\LaTeX}$ file prepared by the author.

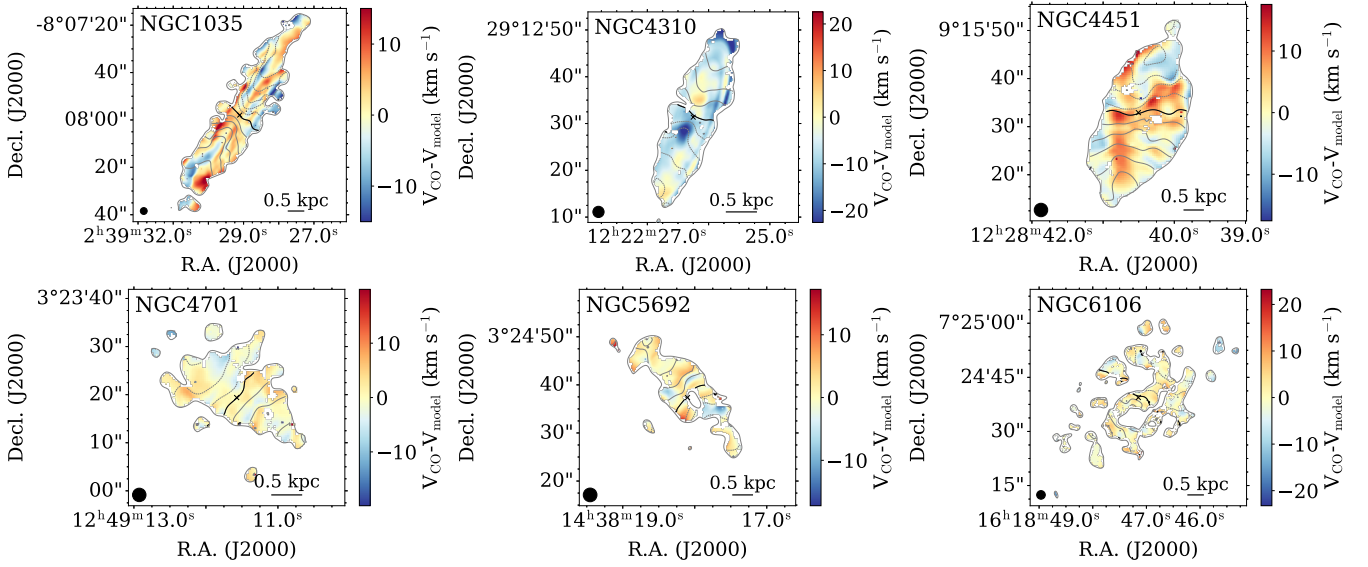


Figure A1. Residual velocity fields, showing the best-fitting harmonic decompositions removed from the observed CO velocity fields. The crosses show the location of the kinematic centre (Table 2). The grey contours surrounding the residual velocity field show SNR = 3 based on the CO peak intensity. The CO velocity map is masked to this level. The black ellipse in the lower left corner shows the FWHM beam size. The grey contours over the residual velocity shows the CO velocity (as in Figure 1) from -100 km s^{-1} to 100 km s^{-1} in 20 km s^{-1} intervals. Solid contours show positive velocities, dashed contours show negative velocities, and the black contour shows $V = 0 \text{ km s}^{-1}$. Note that, unlike Figure 1, the panels are not all cropped to the same angular size.

Table B1. Fitted Dark Matter Density Parameters

Name	ρ_o ($M_\odot \text{ pc}^{-3}$)	r_s (kpc)	β	Y_* ($M_\odot L_\odot^{-1}$)	PA (deg)	i (deg)
NGC 1035	$0.27^{+0.30}_{-0.12}$	$3.0^{+1.5}_{-1.2}$	$0.3^{+0.2}_{-0.2}$	$0.20^{+0.02}_{-0.02}$	145^{+2}_{-2}	80^{+2}_{-3}
NGC 4310	$0.60^{+0.47}_{-0.33}$	$1.8^{+0.8}_{-0.5}$	$-0.4^{+0.5}_{-0.5}$	$0.22^{+0.02}_{-0.03}$	334^{+5}_{-3}	71^{+3}_{-2}
NGC 4451	$0.41^{+0.47}_{-0.24}$	$2.2^{+0.8}_{-0.7}$	$-0.0^{+0.5}_{-0.6}$	$0.22^{+0.02}_{-0.03}$	177^{+4}_{-3}	50^{+3}_{-3}
NGC 4701	$0.73^{+0.77}_{-0.57}$	$1.4^{+1.1}_{-0.7}$	$-0.7^{+1.0}_{-0.9}$	$0.21^{+0.03}_{-0.02}$	230^{+3}_{-4}	49^{+3}_{-3}
NGC 5692	$0.53^{+0.64}_{-0.34}$	$1.6^{+1.4}_{-0.8}$	$-0.1^{+0.9}_{-1.1}$	$0.85^{+0.10}_{-0.12}$	35^{+4}_{-3}	52^{+3}_{-2}
NGC 6106	$0.64^{+0.81}_{-0.57}$	$1.4^{+3.5}_{-0.6}$	$-0.1^{+0.7}_{-0.7}$	$0.21^{+0.03}_{-0.03}$	143^{+3}_{-3}	59^{+3}_{-2}

The density normalisation (ρ_o), radial scale length (r_s), and power-law index (β) are the three fitted parameters in the gNFW profile (Equation 3). The fitted mass-to-light ratio (Y_*), position angle (PA), and inclination (i) agree with the fiducial values listed in Tables 2 and 3 within the uncertainties. The uncertainties are the 68 per cent confidence intervals of the marginalized posterior distributions (Figure B1). See Section 4 for details.

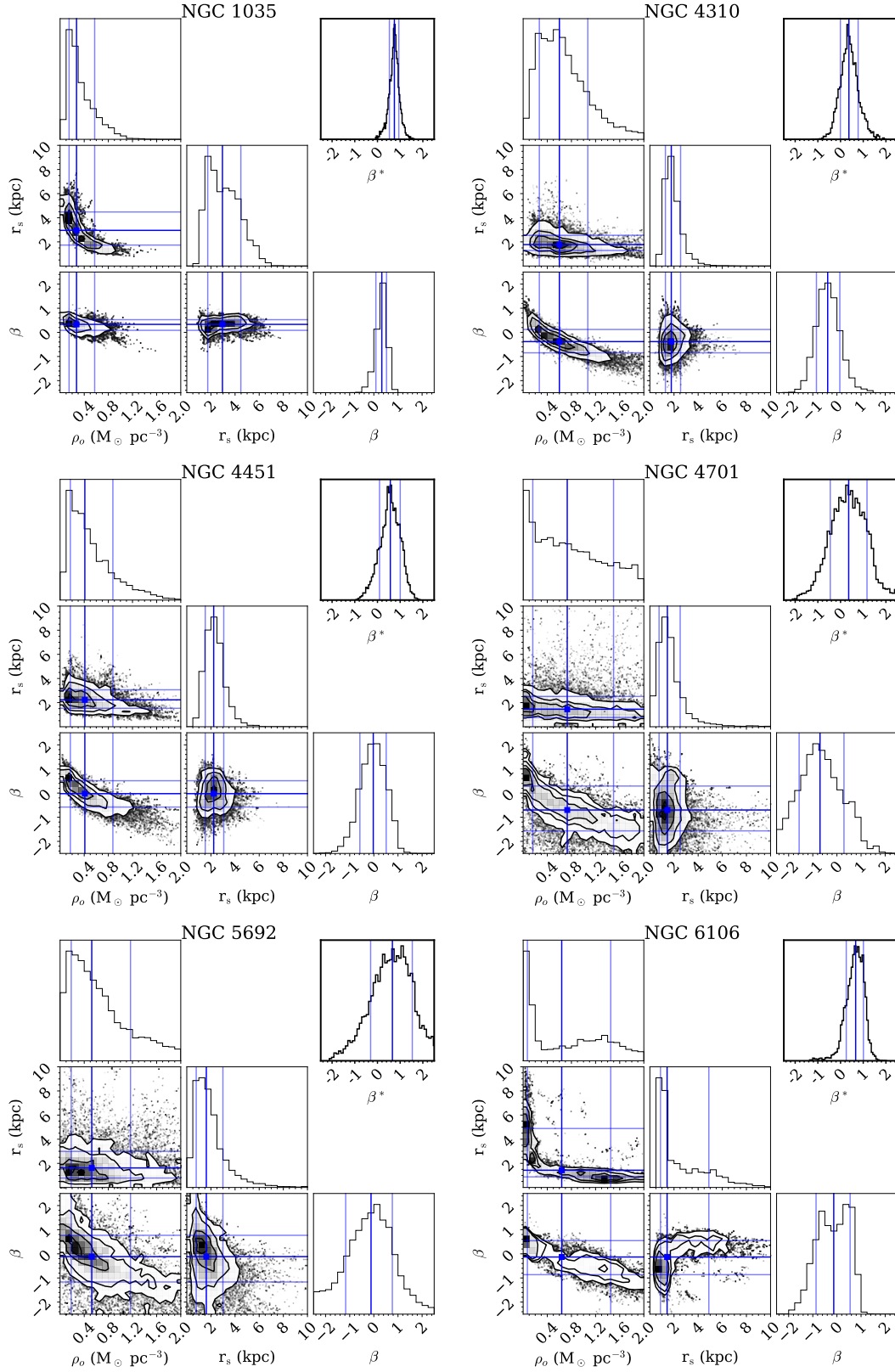


Figure B1. The posterior distributions for ρ_0 , r_s , and β in the gNFW dark matter profile given in Equation 3 are shown in these corner plots. The plots in the upper right corner of each panel with thick outlines show the resulting distribution of β^* . The dark blue lines show the median and the light blue lines show the 16th and 84th percentiles of the marginalized posterior likelihood distributions.

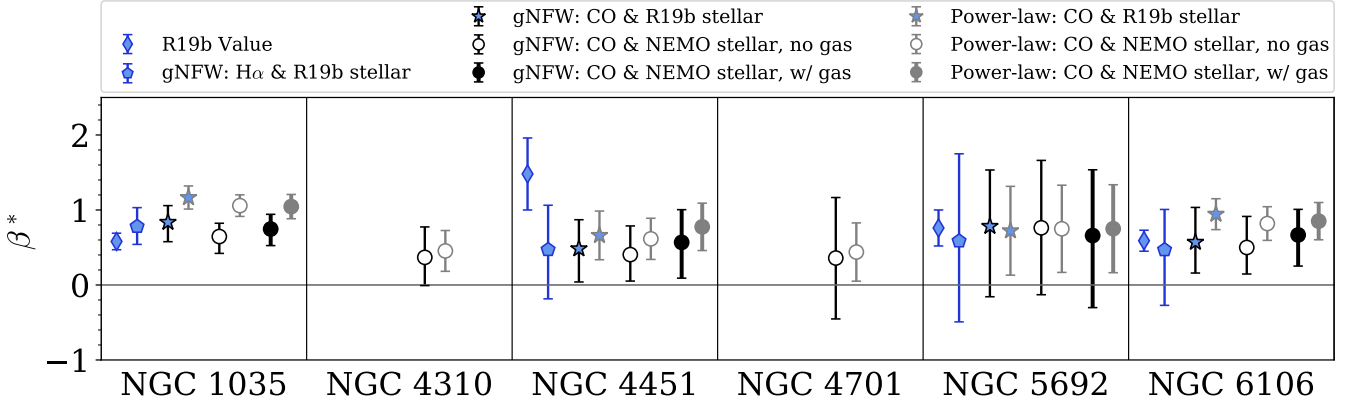


Figure B2. A comparison of the β^* values derived for different forms of the dark matter density profiles. This is the same as Figure 6, but we have added the symbols outlined in grey to this figure, which show the measurements of β^* using a power-law parametrization of the dark matter density profile (Equation B1). Symbol shapes are the same as in Figure 6. In general, the β^* values from the power-law fits agree with those from the gNFW within the uncertainties. Within each galaxy bin, points are artificially offset along the horizontal axis for clarity.